

Strain Engineering of Thermoelectric Properties of Halide Perovskite: A first-Principles Study

Thesis submitted

In partial fulfilment of the requirements for the

Degree of

MASTER OF SCIENCE

in

APPLIED PHYSICS

Submitted By:

**Sumedha Yadav
(23/MSCPHY/55)**

Under the supervision of

Dr. Mukhtiyar Singh

(Delhi Technological University)



Department of Applied Physics

DELHI TECHNOLOGICAL UNIVERSITY

(Formerly Delhi College of Engineering)

Shahbad Daultapur, Main Bawana Road, Delhi-110042,

India

DECLARATION

We, hereby certify that the work which is presented in the Research Work entitled “*Strain Engineering of Thermoelectric Properties of Halide Perovskite: A first- Principles Study*” in fulfilment of the requirement for the award of the degree of Master in Science and submitted to the Department of Applied Physics, Delhi Technological University, Delhi is an authentic record of our own, carried out during a period from May 2024 to May 2025, under the supervision of **Dr. Mukhtiyar Singh**.

The matter presented in this thesis has not been submitted by us for the award of any other degree of this or any other University. The work has been published in peer-reviewed journal Physics Letters A with the following details:

Title of the Paper (I): Optimizing Thermoelectric Performance of Halide Perovskite Ca_3AsBr_3 Through Strain Engineering.

Author names (in the sequence as per research paper): Sumedha Yadav, Sangeeta, Kulwinder Singh, Mukhtiyar Singh.

Name of the Journal: Physics Letters A

Status of paper: Published

Date of paper communication: 18 March 2025

Date of paper acceptance: 4 May 2025

Date of paper publication: 5 May 2025




Sumedha Yadav
(23/MSCPHY/55)

SUPERVISOR CERTIFICATE

To the best of my knowledge, the above work has not been submitted in part or full for any Degree or Diploma to this University or elsewhere. I, further certify that the publication and indexing information given by the students is correct.

Place: Delhi

Date: 09/06/2025



Dr. Mukhtiyar Singh
(Supervisor)

ACKNOWLEDGEMENTS

I want to express my gratitude and indebtedness to **Dr. Mukhtiyar Singh**, Assistant Professor, Department of Applied Physics, Delhi Technological University for their inspiring guidance, constructive criticism, and valuable suggestions throughout the project.

I would also like to thank **Ms. Sangeeta**, Research Fellow, Department of Applied Physics, Delhi Technological University for her mentorship and for sharing her experience and expertise on this subject. I am thankful for her constant guidance and support. I would also like to thank my laboratory members and for their continuous support and understanding. I am also thankful to my family and colleagues for their invaluable support, care, and patience during this project.

Lastly, I would also like to thank the Department of Applied Physics, Delhi Technological University for allowing me to work on this topic.

PARTICIPATION RECORD

Name of Conference: Advanced Functional Materials & Devices (AFMD-2025)

Conference Dates: 2025, March 3-5

Mode of the conference: online

Title of the presentation: A first-principles investigation of thermoelectric properties of a cubic halide perovskite Ca_3NCl_3 .

Venue: ATMA RAM SANATAN DHARMA COLLEGE, NEW DELHI



ABSTRACT

As global energy consumption continues to rise, the conventional energy sources becoming unprecedently more pressing. Moreover, the depletion of conventional fossil fuels and their environmental impact raises serious concerns about long-term sustainability. This challenge makes it essential to explore alternative, renewable energy solutions that can support future energy needs while minimizing ecological harm. Thermoelectric (TE) materials represent one of the most promising avenues for sustainable energy conversion. These materials can harness useful electricity from waste heat and thus have been a research focus in recent years. One such type is halide perovskites with crystal structure of form A_3BX_3 . Many studies have demonstrated how strain and spin-orbit coupling (SOC) reduce the bandgap in halide perovskites, potentially enhancing their TE efficiency.

We investigate structural, dynamical, elastic, electronic, and thermoelectric properties of cubic perovskite halide Ca_3AsBr_3 under the effect of strain using first-principles calculations. It is found to have a direct bandgap of 2.425 eV that further reduces under compressive strain making it an ideal candidate for thermoelectric application. The material satisfies various stability criteria, e.g., dynamical, thermodynamical, and mechanical. The transport calculations show the highest Seebeck coefficient of value $-458.227 \mu\text{VK}^{-1}$ at 700 K for n -type Ca_3AsBr_3 unstrained structure at carrier concentration $1 \times 10^{21} \text{ cm}^{-3}$, which is further enhanced to $-482.366 \mu\text{VK}^{-1}$ for -2% strain. The lattice thermal conductivity of the material is reduced from $1.243 \text{ Wm}^{-1}\text{K}^{-1}$ to $0.627 \text{ Wm}^{-1}\text{K}^{-1}$ at 700 K under 3% strain. This low thermal conductivity, coupled with positive power factor values, results in increased peak thermoelectric figure of merit from 0.36 (unstrained) to 0.56 (+3% strain) at 700 K for an n -type doping concentration of $1 \times 10^{20} \text{ cm}^{-3}$.

TABLE OF CONTENTS

<i>CANDIDATE'S DECLARATION</i>	<i>ii</i>
<i>SUPERVISOR CERTIFICATE</i>	<i>ii</i>
<i>ACKNOWLEDGEMENT</i>	<i>iii</i>
<i>PARTICIPATION RECORD</i>	<i>v</i>
<i>ABSTRACT</i>	<i>vi</i>
<i>TABLE OF CONTENTS</i>	<i>vii</i>
<i>LIST OF TABLES</i>	<i>ix</i>
<i>LIST OF FIGURES</i>	<i>x</i>
<i>LIST OF SYMBOLS AND ABBREVIATIONS</i>	<i>xii</i>
CHAPTER 1	1
INTRODUCTION	1
1.1 Thermoelectric materials and energy harvesting	1
1.1.1 Thermoelectric figure of merit (ZT)	2
1.2 Types of thermoelectric materials	4
1.2.1 Perovskites	
1.3 Introduction to material of this study	
Error! Bookmark not defined.	
CHAPTER 2	8
METHODOLOGY	8
2.1. Computational Methods	8
2.1.1. Density Functional Theory (DFT)	8
2.1.2. Exchange correlation functional	11
2.1.3. Generalised gradient approximation	13
2.1.4. The LAPW method	13
2.1.5. Boltzmann Transport Theory	14
2.2. Computer programs	15
2.2.1 VASP	15
2.2.2 WIEN2k	16
2.2.3 BoltZTraP2	17
2.2.4 AMSET	17
CHAPTER 3	20

<i>RESULTS AND DISCUSSION</i>	20
3. Results and discussion for Ca_3AsBr_3	20
3.1 Structural properties	20
3.2 Computational details	21
3.3 Stability Analysis	23
3.4 Electronic Properties	27
3.5 Thermoelectric Properties	30
<i>CONCLUSION AND FUTURE SCOPE</i>	42
<i>REFERENCES</i>	43
<i>PROOF AND SCOPUS INDEXING</i>	49
<i>PLAGIARISM</i>	51

LIST OF TABLES

Table 1: The optimized lattice parameters (in Å), Volume of the unit cell (in Å ³), and bond lengths (in Å) of Ca ₃ AsBr ₃ , along with available experimental data.....	21
Table 2: The elastic constants C_{11} , C_{12} , and C_{33} are in GPa, G_v , G_r , G_h , E , and B are in GPa, Poisson's ratio, Pugh's ratio, and A are dimensionless and melting temperature (K) corresponding to all compressive and tensile strains (in %)......	24
Table 3: Bandgaps for different strains.....	27

LIST OF FIGURES

Different sources of waste heat energy	2
The theme of Density functional theory	9
Scattering of particles in a crystal structure	15
The Logo of VASP	17
The Logo of WIEN2k software	17
The Logo of AMSET	20
(a) Unit crystal structure (Blue, Green, and orange colour represent Ca, As, and Br atoms, respectively) (b) Brillouin zone of Ca_3AsBr_3	20
Plot for the ground state energy with respect to the k -mesh varied in x -, y -, and z -directions by keeping $kx = ky = kz$.	21
(a) The phonon dispersion curve of unstrained Ca_3AsBr_3 and (b) Phonon Density of states (c) phonon dispersion curve of Ca_3AsBr_3 under strain -3% (d) phonon dispersion curve of Ca_3AsBr_3 under strains $+3\%$	26
Electronic band structures and density of states of unstrained Ca_3AsBr_3 with and without SOC	28
Electronic band structures of Ca_3AsBr_3 with (upper panel) and without SOC (lower panel) under compressive strains	28
Electronic band structures of Ca_3AsBr_3 with (upper panel) and without SOC (lower panel) under tensile strain	29
Seebeck coefficient vs temperature for different carrier concentrations for different strains.	32

Scattering rates and carrier mobility due to different scatterings by varying the carrier concentration of Ca_3AsBr_3 for both p -type and n -type	33
Electrical conductivity vs temperature for different carrier concentrations for different strains 0%, $\pm 1\%$, $\pm 2\%$, and $\pm 3\%$	34
Electronic thermal conductivity vs temperature for different carrier concentrations for different strains	35
Power factor vs temperature for different carrier concentrations for different strains.	36
Lattice thermal conductivity for various strains at temperatures 300 to 700 K	37
(a-c) Phonon group velocity, (d-f) Mode Grüneisen parameter (g-i) phonon lifetime corresponding to all phonon modes as a function of frequency for the unstrained and $\pm 3\%$ strained Ca_3AsBr_3 .	39
ZT value for various strains for 300-700 K temperature for fixed carrier concentrations for 0%, +3%, -3% strains	40
ZT value for various concentrations for 300-700 K temperature for different carrier strains $\pm 1\%$ and $\pm 2\%$	41

LIST OF SYMBOLS AND ABBREVIATIONS

Acronym/Symbol	Full Form
TE	Thermoelectric
ZT	Thermoelectric figure of merit
DFT	Density Functional Theory
TB-mBJ	Tran Blaha modified Becke Johnson
LDA	Local Density Approximations
GGA	Generalised Gradient Approximations
PBE	Perdew-Burke-Ernzerhof
BTE	Boltzmann transport equations
DOS	Density of States
PDOS	Projected Density of States
CRTA	Constant relaxation time approach
E_g	Band-Gap
Å	Angstrom
eV	electron-volt
E_f	Formation energy
RBA	Rigid band approximation
Γ	Gamma
Ca	Calcium
Br	Bromine
As	Arsenic
LAPW	Linear augmented plane wave

C_{11}, C_{22}, C_{44}	Elastic constants
CBM	Conduction band minimum
VBM	Valence band maximum
τ	Constant relaxation time
KSE	Kohn-Sham equations
VB	Valence band
CB	Conduction Band
Ca_3AsBr_3	Calcium Arsenide Bromide
PAW	Projected Augmented wave
μ	mobility
L	Lorenz number

CHAPTER 1

INTRODUCTION

1.1 Thermoelectric materials and energy harvesting

In a world grappling with excessive fossil fuel consumption and its detrimental environmental impacts, achieving a net zero target requires balancing greenhouse gas emissions with removal efforts. To achieve this, developing clean and secure energy alternatives is imperative. New technologies can play a pivotal role in energy generation and storage. These encompass diverse areas such as photovoltaics, wind and water turbines, and energy-efficient technologies like low-loss electronics, piezoelectrics and thermoelectrics (TEs) [1–5]. Thermoelectricity refers to phenomena that involve the direct and thermodynamically reversible exchange of thermal energy to electricity or vice versa. The Seebeck, Peltier, and Thomson effects are three distinct phenomena that make up thermoelectricity and are named after the researchers who first identified them in the late 19th century. TE materials, for instance, can efficiently convert waste heat into usable electrical energy, powering TE generators. TE devices show unique advantages compared to other energy conversion devices, including stability, long service life, and noiselessness. TE materials harness temperature differentials to produce electrical energy, offering a means of achieving fully electric heating and cooling technology devoid of mechanical components or refrigerants. An additional benefit of this technology lies in its capability to capture residual heat from various phenomena and convert them into electricity. Considering that approximately 2/3 of primary energy is dissipated as heat, the utilization of thermoelectric materials holds the potential to efficiently capture and convert a significant portion of this wasted heat into valuable electrical power. Thermoelectric (TE) materials represent one of the most promising avenues for sustainable energy conversion. These materials can harness useful electricity from waste heat and thus have been a research focus in recent years [6].

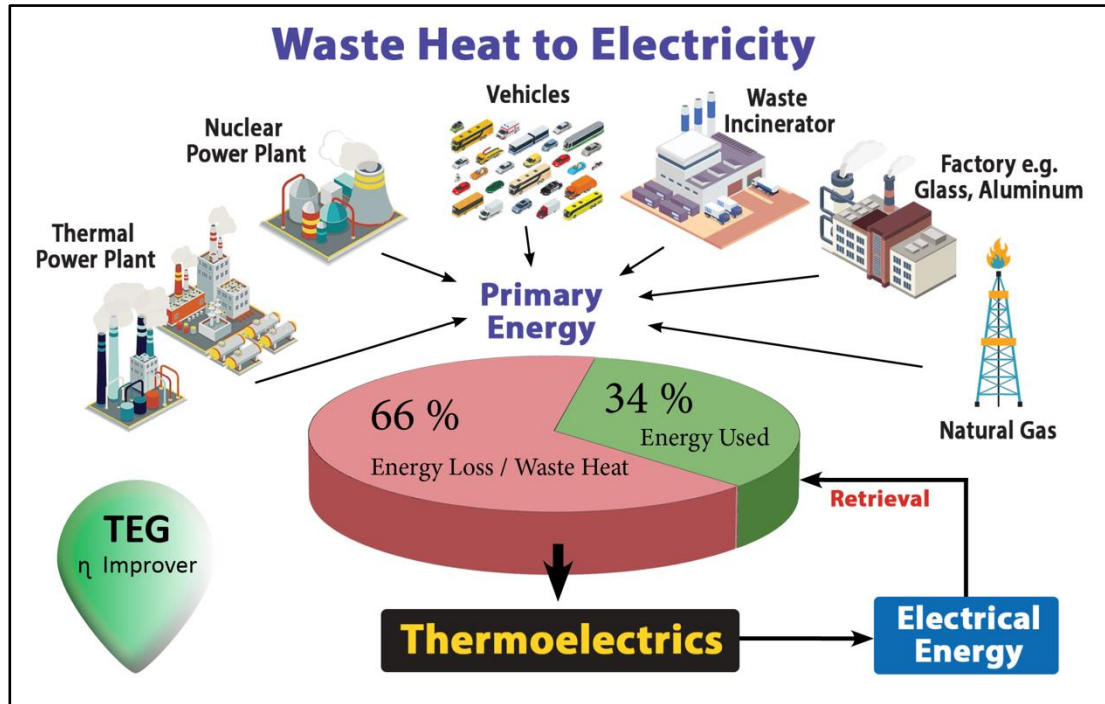


Figure 1: Different sources of waste heat energy

1.1.1 Thermoelectric figure of merit (ZT)

ZT represents the efficiency of TE material and can be calculated from the formula $ZT = S^2\sigma T/\kappa$, S denotes the Seebeck coefficient, σ represents electrical conductivity, where T is the absolute temperature, and κ encompasses the combined effects of electronic (κ_e) and lattice (κ_l) contributions to thermal conductivity. Achieving an optimal ZT necessitates a high power factor ($S^2\sigma$) and reduced κ value. A significant challenge lies in optimizing $S^2\sigma$ and κ_e , as they are interdependent with each other through the carrier concentration. Various strategies have been devised to overcome this challenge to decouple these parameters. These include increasing the power factor via carrier concentration adjustments, tuning band structures, and reducing lattice thermal conductivity through dimensional reduction or introducing defects [7-12].

The Seebeck effect is the phenomenon of the development of electromotive force (emf) across two sites of material as their temperatures differ, the emf is known as the thermoelectric emf. The Seebeck coefficient is the ratio of this emf and the corresponding temperature change in temperature . A thermocouple gauges the difference between the potential at the hot and cold ends of two different materials. The potential difference between the cold and hot ends is proportional to the difference in temperature across these ends. The first experiments revealing this effect were performed by Alessandro Volta in 1794. The Seebeck effect, like any other emf, produces measurable currents or voltages. $J = \sigma (-\nabla V + E_{emf})$ is the current density(local), where σ conductivity and V is the local electrical potential. The Seebeck effect arises from a local electromotive field,

$E_{emf} = -S\nabla T$, where S is a parameter that depends locally and ∇T is the temperature gradient. The Seebeck coefficient depends strongly on the composition of the material and, in general, also varies with the temperature. The Seebeck coefficient for ordinary materials at room temperature generally lies in the $-100 \mu\text{V/K}$ to $+1,000 \mu\text{V/K}$ range.

Electrical conductivity (σ) is the measurement of the current carried by a material . It is an intrinsic property of a material and depends on the material properties. The electrical conductivity of a metallic conductor increases progressively as the temperature decreases. Superconductors exhibit a remarkable phenomenon wherein their resistance drops to zero below a critical temperature. Consequently, a current can flow through a superconducting wire loop without the need for applied power.

In various systems, conduction is facilitated by either band holes or electrons. In the case of electrolytes, the movement of entire ions takes place, transporting their net electrical charge. For electrolytic solutions, the conductivity of the material is significantly influenced by the concentration of ionic species.

The lattice component of thermal conductivity (k_l) refers to the heat transmission through the vibrations of lattice ions within a solid. Delving into the physics governing the heat conduction process allows for a thorough and nuanced comprehension of the nature of lattice vibrations in solids. Among a material's fundamental and crucial

physical parameters, its thermal conductivity holds significance. It emerges from phonons of all frequencies. Its manipulation has inflicted a huge variety of technical applications that Incorporate the control of temperature in electrical, chemical, mechanical and even nuclear systems materials for thermal barriers and insulation; enhanced thermoelectric materials for increased efficiency; and sensors and transducers.

A profound understanding of thermal conductivity proves crucial in the thermal management of diverse systems, including mechanical, electrical, chemical, and nuclear systems. Lattice thermal conductivity plays a key feature in enhancing the ZT values Materials that have ultralow lattice thermal conductivity possess high ZT values, especially two-dimensional materials.

1.2 Types of Thermoelectric Materials

1. Semiconductor Materials

Semiconductors are the most widely studied and used materials for thermoelectric applications due to their high efficiency compared to metals and insulators. The properties of these materials can be tuned by doping and other modifications.

Eg: Bismuth Telluride (Bi_2Te_3), Lead Telluride (PbTe), Silicon-Germanium (SiGe) Alloys, Skutterudites.

2. Half-Heusler Alloys

Half-Heusler Alloys have a structure similar to that of the Heusler alloys but with a different stoichiometry. These materials exhibit good thermoelectric performance over a wide temperature range (500–800 K). They offer a good balance between electrical conductivity and low thermal conductivity, making them suitable for power generation.

3. Nanostructured Thermoelectric Materials

Nanostructuring can significantly enhance the thermoelectric performance by reducing the thermal conductivity without severely impacting electrical conductivity. This is often achieved through the creation of nanowires, quantum dots, or superlattices.

4. Organic Thermoelectric Materials

Organic materials have recently been of interest because they are flexible, easy to process, and can be manufactured at low cost. However, they generally have lower thermoelectric performance than inorganic materials. Eg: Conducting Polymers, Organic-Inorganic Hybrid Materials

5. Perovskite-Based Thermoelectric

Perovskite materials in particular, halide perovskites, have attracted much attention as potential thermoelectrics because of their ability to be engineered to possess tunable electronic properties and low thermoelectric conductivity.

1.2.1 Perovskite Materials

Perovskite materials are a group of compounds that crystallize with the mineral perovskite structure, CaTiO_3 . The perovskite structure is probably one of the most versatile and important crystal structures in materials science, known for its unique physical properties and versatility. These materials can be inorganic, organic-inorganic hybrid, or fully organic. They all show interesting and useful properties, such as superconductivity, ferroelectricity, magnetism, and efficient light absorption.

Halide Perovskite Materials

Halide perovskites are a sub-class of perovskite materials wherein the "X" in the ABX_3 or A_3BX_3 structure is a halide ion (chloride, bromide, or iodide). The interest in these materials has been considerable in the past few years, with an emphasis on photovoltaic solar cells, LEDs, lasers, and photodetectors. The halide perovskites have demonstrated notable properties, including high absorption efficiencies, tunable band gaps, and ease of fabrication; therefore, they are regarded as among the most promising candidates for next-generation optoelectronic applications.

Structure of Halide Perovskites

The ABX_3 structure in halide perovskites consists of:

A-site: Large organic or inorganic cation

B-site: A small metal cation

X-site: A halide anion, such as chloride (Cl), bromide (Br), or iodide (I).

The perovskite structure forms a 3D framework where the B cations, such as Pb^{2+} , are surrounded by halide ions, such as I^- , and the A

cations are located in the voids between these octahedral units. This structure is responsible for their excellent optoelectronic and thermoelectric properties, such as high electron mobility and efficient charge transport.

Inorganic Halide Perovskites:

Cesium Lead Iodide (CsPbI_3) is a quite notable example of an inorganic halide perovskite. These materials are purely inorganic, which often leads to enhanced thermal stability compared to organic-inorganic hybrids. It has properties such as enhanced stability and reduced susceptibility to moisture, but they may require higher temperatures for efficient processing.

1.3 Introduction to material of this study

The inorganic materials like Bi_2Te_3 (effective at room temperature), chalcogenides and half Heusler compounds (suited for mid-to-high temperatures like 400–800 K), skutterudites and clathrates (500–900 K), Zintl phases (covering various temperature ranges for different compositions ~300–900 K), and oxide perovskites (best for high temperatures ~700–1200 K) are widely used as efficient TE materials across different temperature regimes [13–16]. However, the scarcity of raw materials such as tellurium and lead, along with the complex and costly fabrication processes, significantly hinder the commercialization of such inorganic TE materials. Inorganic perovskites are low-cost efficient materials emerging as promising materials in science and technology development [17]. Owing to their unique crystal structure ABX_3 (with A, and B as cations of different sizes and X as an anion that bonds with both cations) perovskite materials are widely used in chemistry, physics, and other fields with successful synthesization of hundreds of distinct materials that make up the large perovskite family including conductors, semiconductors, and insulators [18]. These perovskites reveal many intriguing properties such as high TE power, ferroelectricity, superconductivity, spin-dependent transport, etc. [19–23]. Further, exploring alternative perovskite frameworks A_3BX_3 such as Sr_3NCl_3 , Ca_3PX_3 , and Sr_3PBr_3 , which naturally exhibit cubic symmetry like traditional ABX_3 perovskites, offers several advantages, including greater structural stability, improved tunability of

electronic, and optical properties and can show great promise for TE applications [24–27]. For instance, Ba_3AsX_3 ($X = \text{F}, \text{Cl}$) has demonstrated ZT values of 0.92 and 0.82, respectively, which result from its favorable σ , optimized S , and a stable perovskite framework that supports efficient charge transport [24].

Advancing TE technology requires materials with inherently low κ_l . Recently, Tranås et al. investigated a wide range of materials using a machine-learning model and first-principles calculations and identified some materials that have intrinsically low κ_l [28]. Among the identified candidates, Calcium Arsenide Bromide (Ca_3AsBr_3), a cubic halide perovskite, might stand out as a promising TE material, which motivated us to select it for further investigation. This material was first studied experimentally in 1984 by Hadenfeldt et al. [29], where its thermal behavior, was also analyzed. Recently, theoretical work has explored some properties of Ca_3AsBr_3 , but its TE performance remains unexplored [30]. Many studies have demonstrated how strain and spin-orbit coupling (SOC) reduce the bandgap in halide perovskites, potentially enhancing their TE efficiency [31,32]. Strain influences S and σ by modifying the bandgap or enhancing the density of states (DOS) near the Fermi level [33].

In this study, we have confirmed various stability parameters of halide perovskite Ca_3AsBr_3 , like mechanical, dynamical, thermodynamical, and calculated its electronic properties. TE properties of Ca_3AsBr_3 were studied under the effect of compressive and biaxial strain using first-principles calculation with semiclassical Boltzmann transport theory; also, the relaxation time and mobilities of carriers were calculated using the AMSET code. In the present study, we also showed carrier doping as an effective way to enhance TE performance by analyzing properties at different carrier concentrations for both p -type and n -type material. Further insights into the lattice dynamics of the material by observing group velocity, Grüneisen parameter, and phonon lifetime helped in the better analysis of the thermal properties of the investigated structures. Our calculated ZT is enhanced for +3% strain at 700 K compared to the unstrained structure, but it is still not that high and thus leaves scope for further material optimization.

CHAPTER 2

METHODOLOGY

2.1. Computational Methods

2.1.1. Density Functional Theory (DFT)

DFT gives us a powerful mathematical tool to analyse the many-body system's electronic properties, including molecules, atoms, and even condensed matter. The theory enables us to determine the properties of such systems based on their spatially dependent electron density, making it a remarkably versatile tool within the field of computational condensed matter physics [56].

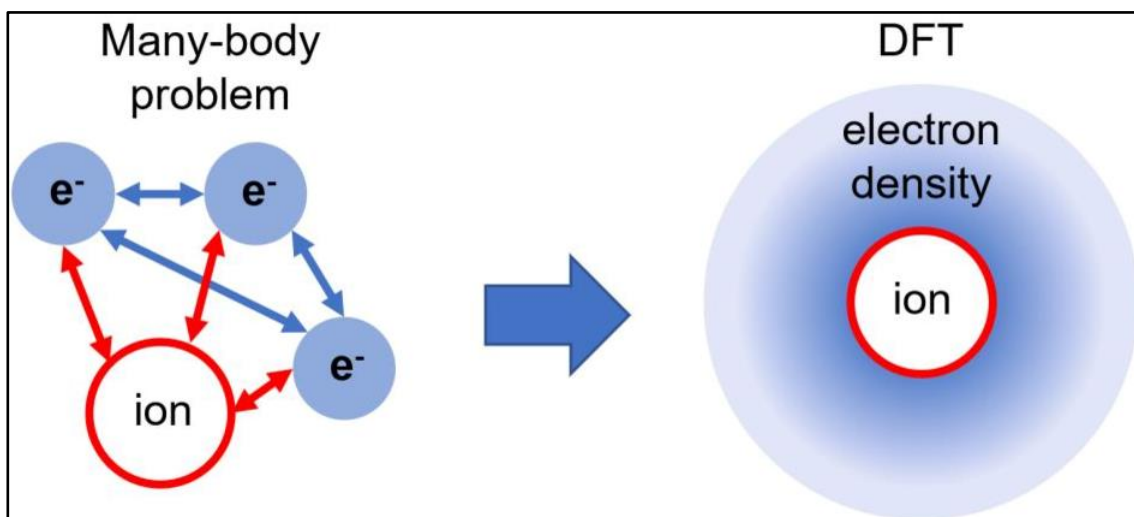


Figure 3: Represents the theme of Density functional theory

Derivation and formalism

The Hohenberg-Kohn theorem highlights a main aspect of the function, The electron density that takes part in minimizing the overall functional energy corresponds to the

real electron density associated with the complete solution of the Schrödinger equation. If we were acquainted with the functional form which was accurate, we could adjust the electron density iteratively until the functional's energy is minimized, providing a method for determining the pertinent electron density. In practice, we apply the variational principle using approximate functional forms. Using the Born-Oppenheimer approximation, treated molecule's nuclei or clusters are taken to be stationary, producing a static potential V where electrons are travelling. Then, a wavefunction $\Psi(\mathbf{r}_1, \dots, \mathbf{r}_N)$ meeting the many-electron time-independent Schrödinger equation can be used to describe a stationary electronic state.

$$\hat{H} \Psi = [\hat{T} + \hat{V}_{nu-e} + \hat{V}_{e-e}] \Psi = [\sum_{i=1,2,\dots,N} ((-\hbar^2/2m_i) \nabla_i^2) + \sum_{i=1,2,\dots,N} (V_{nu-e}(\mathbf{r}_i)) + \sum_{i<j} V_{e-e}(\mathbf{r}_i, \mathbf{r}_j)] \Psi = E \Psi \quad (1)$$

Where, for the system of N electrons, \hat{H} (Hamiltonian operator), E denotes the overall energy, \hat{T} denotes the kinetic energy operator, \hat{V}_{nu-e} denotes the potential energy operator corresponding to the external field due to the positively charged nuclei and \hat{V}_{e-e} denotes the operator corresponding to inter-electronic interactions. The operators \hat{T} and \hat{V}_{e-e} are identical for any N -electron system and for this reason, are called universal operators. The operator \hat{V}_{nu-e} depends on the specifics of a particular system. Owing to the inter-electronic interaction term corresponding to \hat{V}_{e-e} ,

The application of DFT allows to mapping of the many-particle problem, containing \hat{V}_{e-e} , to a one-particle problem free from \hat{V}_{e-e} . The electron density $n(\mathbf{r})$, a crucial quantity in DFT, is given for a normalized Ψ by

$$n(\mathbf{r}) = N \int d^3\mathbf{r}_2 \dots \int d^3\mathbf{r}_N \Psi^*(\mathbf{r}, \mathbf{r}_2, \dots, \mathbf{r}_N) \Psi(\mathbf{r}, \mathbf{r}_2, \dots, \mathbf{r}_N) . \quad (2)$$

$$\Psi_0 = \Psi[n_0], \quad (3)$$

The fact that the wavefunction is a functional of $n_0(\mathbf{r})$ immediately leads to the finding that the expectation value of an observable \hat{O} when the system is in the ground state is also a functional of $n_0(\mathbf{r})$

$$O[n_0] = \langle \Psi[n_0] | \hat{O} | \Psi[n_0] \rangle. \quad (4)$$

Further, it is possible to explicitly write the contributions due to the external potential $\langle \Psi[n_0] | \hat{V}_{nu-e} | \Psi[n_0] \rangle$ as:

$$V_{nu-e}[n_0] = \int V_{nu-e}(\mathbf{r}) n_0(\mathbf{r}) d^3\mathbf{r}. \quad (5)$$

This argument can be extended and the contribution due to the external potential may be expressed as:

$$V_{nu-e}[n] = \int V_{nu-e}(\mathbf{r}) n(\mathbf{r}) d^3\mathbf{r}. \quad (6)$$

$T[n]$ and $U[n]$ are referred to as universal functionals, but $V_{nu-e}[n]$ being dependent on the specifics of the given system is referred to as a non-universal functional. Having specified a system, the minimization of the functional

$$E[n] = T[n] + V_{e-e}[n] + \int V_{nu-e}(\mathbf{r}) n(\mathbf{r}) d^3\mathbf{r} \quad (7)$$

The objective is to minimize the energy functional concerning $n(\mathbf{r})$. The minimization process of the energy functional results in the determination of the ground-state electron density ($n(\mathbf{r})$), subsequently determining all other observables associated with the ground state.

The Lagrangian method of multipliers offers a solution to the variational problem of minimizing the energy functional $[E[n]]$. To initiate the process, we examine an energy functional that does not incorporate the inter-electronic interaction energy.

$$E_{eq}[n] = \langle \Psi_{eq}[n] | \hat{T} + \hat{V}_{eq} | \Psi_{eq}[n] \rangle, \quad (8)$$

where \hat{T} denotes the operator corresponding to the kinetic energy, and \hat{V}_{eq} denotes the operator corresponding to the equivalent potential in which the particles are travelling. E_{eq} can be used to generate the following Kohn-Sham equations for this auxiliary, noninteracting system:

$$[-(\hbar^2/2m) \nabla^2 + V_{eq}(\mathbf{r})] \varphi_i(\mathbf{r}) = \varepsilon_i \varphi_i(\mathbf{r}), \quad (9)$$

which gives the orbitals φ_i that mimic the electron density $n(\mathbf{r})$ of the actual many-particle system

$$N(\mathbf{r}) = \sum_{i=1,2,\dots,n} |\varphi_i(\mathbf{r})|^2. \quad (10)$$

The equivalent single-body potential may be expressed as

$$V_{eq}(\mathbf{r}) = V_{nu-e}(\mathbf{r}) + \int (n(\mathbf{r}')/|\mathbf{r}-\mathbf{r}'|) d^3\mathbf{r}' + V_{EC}[n(\mathbf{r})], \quad (11)$$

first term $V_{nu-e}(\mathbf{r})$ is the extrinsic potential, the second term is the Hartree term expressing the inter-electronic Coulombic interaction, and the third term V_{EC} denotes the exchange-correlation potential. Here the entirety of the many-body interactions is incorporated in the exchange-correlation potential V_{EC} . The task of finding the solution to the KSE is approached in an iterative self-consistent fashion. Initially, a starting guess for $n(\mathbf{r})$ is made following which the corresponding V_{eq} is determined and the Kohn-Sham equations are solved for the φ_i . Using these φ_i 's a new electron density is determined and the aforementioned sequence of steps is repeated. Up until convergence, this process is repeated [57].

2.1.2. Exchange correlation functional

It is guaranteed that the exchange-correlation functional has a correct shape by the Hohenberg-Kohn theorem, which remains unknown. However, there is a specific scenario in which we can precisely derive this functional: the uniform electron gas. In this instance, we assume that the $n(\mathbf{r})$ remains the same at all points in space, denoted,

$n(\mathbf{r})$ 1/4 constant. While this seems limited in relevance to real materials, which exhibit variations in electron density defining chemical bonds and contributing to material properties, the uniform electron gas offers a practical means to apply the KSE. Using this method, the known exchange-correlation potential from the uniform electron gas at the electron density observed at that place is set at each position.. This is accomplished by analysing the same system employed in the KSE. Through the K-S formulation of DFT, the total energy is expressed as follows

$$E_{tot, KS-DFT} = - \left(\frac{1}{2} \right) \sum_i \int \Psi_i^* (\mathbf{r}) \nabla^2 \Psi_i(\mathbf{r}) d^3\mathbf{r} - \sum_J \int \left(Z_J / |\mathbf{r} - \mathbf{R}_J| \right) n(\mathbf{r}) d^3\mathbf{r} + \left(\frac{1}{2} \right) \iint \left(n(\mathbf{r}) n(\mathbf{r}') / |\mathbf{r} - \mathbf{r}'| \right) d^3\mathbf{r} d^3\mathbf{r}' + E_{EC} + \left(\frac{1}{2} \right) \sum_{I \neq J} \left(Z_I Z_J / |\mathbf{R}_I - \mathbf{R}_J| \right) \quad (12)$$

The first right-hand term side expresses the electronic non-interacting kinetic energy, the next term expresses the nuclei-electron interaction energy followed by the Coulombic inter-electronic interaction energy, the next term expresses the exchange-correlation energy and the fifth term expresses the inter-nuclei interaction energy. The orbitals and the electron density $n = \sum |\Psi_i|^2$ are attained by self-consistently solving the Kohn-Sham equations: Self-consistently solving KSE yields the orbitals Ψ_i and the electron density $n = \sum |\Psi_i|^2$ that may be used for the determination of $E_{tot, KS-DFT}$:

$$\left(- \left(\frac{1}{2} \right) \nabla^2 - \sum_J \left(Z_J / |\mathbf{r} - \mathbf{R}_J| \right) \right) + \int \left(n(\mathbf{r}') / |\mathbf{r} - \mathbf{r}'| \right) d^3\mathbf{r}' + v_{EC}(\mathbf{r}) \Psi_i(\mathbf{r}) = \varepsilon_i \Psi_i(\mathbf{r}). \quad (13)$$

The exchange-correlation energy functional E_{EC} and potential $v_{EC} = \delta E_{EC} / \delta n$ are the only terms in $E_{tot, KS-DFT}$, and the Kohn-Sham equations that are not precisely known. As a result, the correctness of the estimated characteristics is primarily dependent on the E_{EC} and v_{EC} estimates. A multitude of exchange and correlation approximations have been developed. They can be divided into several categories, including GGA, LDA, meta-generalized gradient approximation (meta-GGA), and hybrid approximations [58].

2.1.3. Generalised gradient approximation

When the correlation functional was expanded in terms of the gradient of the density through the Taylor series and terminated it at some order. Such an approximation is known as gradient expansion approximation (GEA), this was initiated by Herman in 1969. It turned out that such an approximation often gave worse results and did not provide any improvement over local density approximations. This was because the gradients of the density in the real system become very large; as a result, such expansions break down. It was also found that the GEA does not satisfy most of the sum rules. Later only, it was realized that there was no need of such an expansion and it was possible to construct exchange-correlation functional, which was a functional of density as well as its gradient and satisfied the sum rules. This could be written as [59]

$$E_{xc} [n_{\uparrow}, n_{\downarrow}] = \int d^3 r f(n_{\uparrow}(r), n_{\downarrow}(r), \nabla n_{\uparrow}, \nabla n_{\downarrow}) \quad (14)$$

2.1.4. The LAPW method -

The LAPW method is one of the most precise methods for finding crystal electrical structures. It is based on DFT and addresses exchange and correlation using approaches such as the local spin density approximation (LSDA). There are several types of LSDA potentials, and new advancements employing the generalized gradient approximation (GGA) are also available. On either a scalar or a vector relativistic method, relativistic effects in valence states can be incorporated. Or a second variational technique that takes spin-orbit coupling into account. The core states are treated in their entirety relativistically.

2.1.5. Boltzmann Transport Theory

The Boltzmann transport theory expresses the interplay between the driving effect of the extrinsic fields and the dissipative effect of scattering of carriers by phonons and defects. This theory can be used to explore how the thermal equilibrium distribution

of carriers changes in the presence of external forces and electron scattering mechanisms.

The Boltzmann equation, which is presented below, serves as the foundation for the analysis of solid-state transport characteristics.

$$\partial f / \partial t + v \cdot \nabla_r f - (e / \hbar) \varepsilon \cdot \nabla_k f = (\partial f / \partial t)_s \quad (15)$$

The drift terms are on the left-hand side and the terms on the right are scattering term. Let us assume that these scattering processes are immediate and can change the electron's local state from k to k' . Define $W(k, k')$ as the scattering rate between the k and k' states. if k' is empty and k state is filled. The rate at which scattering alters the distribution function $f_k(v)$ is

$$(\partial f(\mathbf{r}, \mathbf{k}, t) / \partial t)_s = (V / (2\pi)^3) \int d\mathbf{k}' \{ [1 - f(\mathbf{r}, \mathbf{k}, t)] w_{k'k} f(\mathbf{r}, \mathbf{k}', t) - [1 - f(\mathbf{r}, \mathbf{k}', t)] w_{kk'} f(\mathbf{r}, \mathbf{k}, t) \} \quad (16)$$

the $2\pi^3$ denominator originates from the count of permissible states within a k -space d^3k' . In the integral, the initial term signifies the electron rate transition from ' k' ' state (hence the factor ' $f_{k'}$ ') to k which is unoccupied hence the factor $(1 - f_k)$. The subsequent term accounts for the loss aspect. In a state of steady equilibrium, there is no alteration in the $f_k(v)$, and the overall summation of the partial derivative terms remains constant.

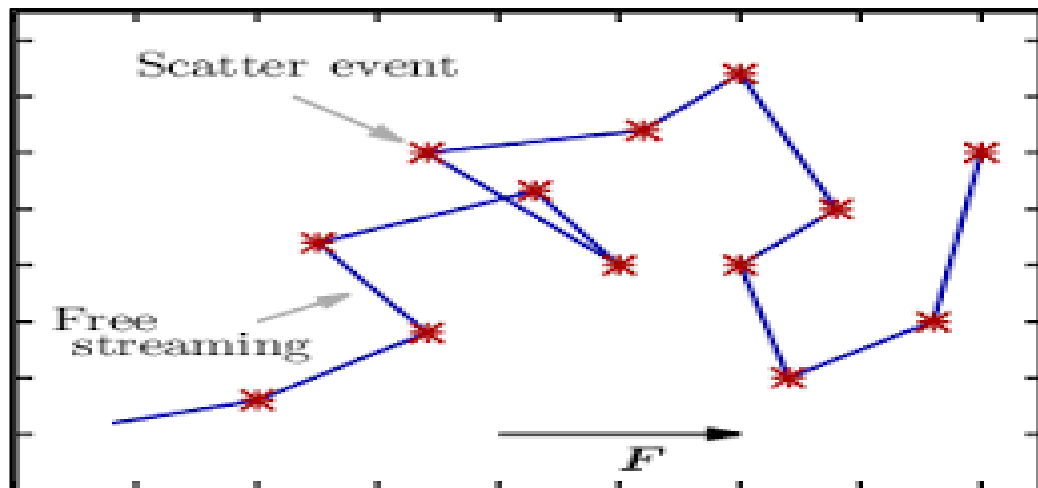


Figure 4: Scattering of particles in a crystal structure

2.2. Computer programs

2.2.1 VASP

The Vienna Ab Initio Simulation Package (VASP), is a tool employed for conducting quantum mechanical calculations. This involves the use of PAW, coupled with a plane wave basis set. VASP solves the many-body Schrödinger equation approximately by solving the KSE (in the framework of DFT) or by solving the Roothaan equations (in the framework of the Hartree-Fock approach). Additionally, certain hybrid functionals that inherit aspects from both the Hartree-Fock approach and the DFT are also available. VASP calculates key quantities through plane wave basis: single-electron orbitals, charge density, and local potential. The exchange the electrons and ions is either expressed with the help of the PAW method or with the help of norm-conserving or ultrasoft pseudopotentials[60].

VASP carrier out calculations using 4 necessary input files, which are

1. **INCAR:** This file is used to determine what kind of calculation has to be done on the investigated system There are certain tags specified in the INCAR file which we have to set to select a certain algorithm and set the parameters.
2. **POSCAR:** this file gives the details of the system that we study. it consists of the atomic positions in the unit cell and the translational vectors.
3. **POTCAR:** This file consists of the pseudopotential for every single atomic species which is present in Mendeleev's
4. **KPOINTS:** This file sets the mapping for the irreducible Brillouin zone in the crystal reciprocal lattice structure

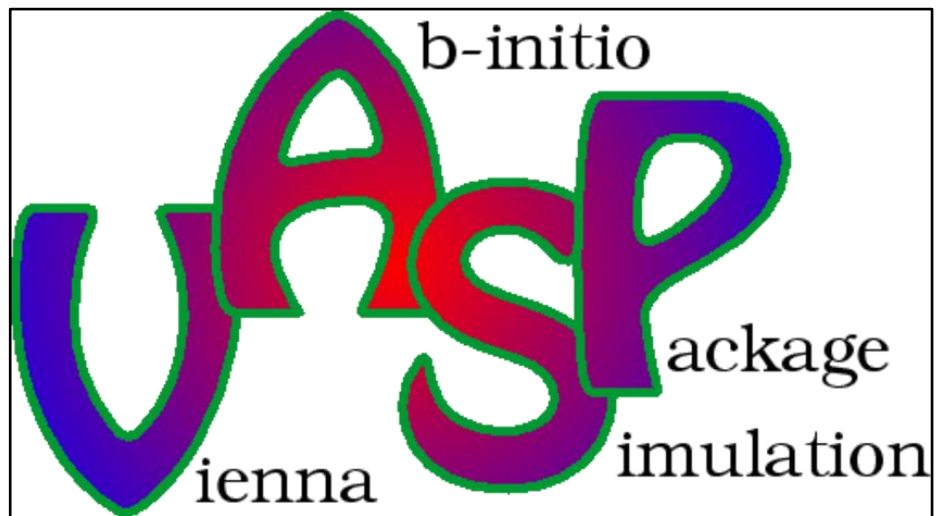


Figure 5: The Logo of VASP

2.2.2 WIEN2k

WIEN2k is a program designed to calculate the electronic structure of solids DFT. It utilizes the most precise methods for determining band structure: local orbitals (Lo) combined with the full-potential LAPW method. WIEN2k is an all-electron system that includes several features and accounts for relativistic effects.

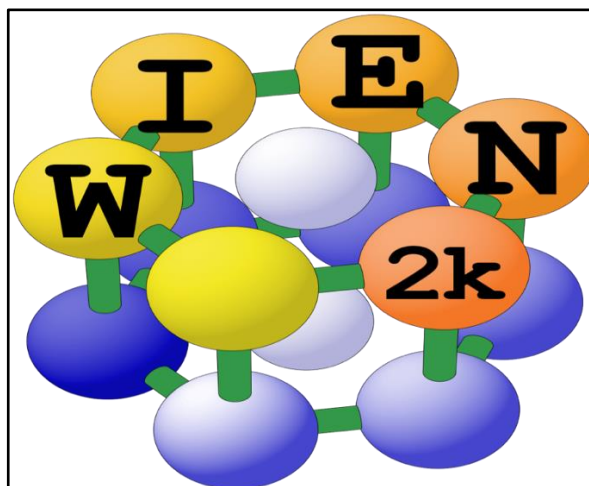


Figure 6: The logo of WIEN2k software

2.2.3 BoltZTraP2

BoltZTraP2 is a software that utilises the linearized BTE to determine smoothed Periodic function Fourier expressions and their accompanying transport coefficients for extended systems. It utilizes the band structure,

The program may be used as a Python module or through a command-line interface.

One of the most important merits of the procedure employed by BoltZTraP2 is the computational ease in the evaluation of transport coefficients due to its ability to efficiently compute group velocities of quasi-particles.

BoltZTraP is frequently used in conjunction with the CRTA. Within the CRTA, the S becomes independent of the scattering rate. As a result, it is possible to obtain the Seebeck coefficient. The combination of CRTA and RBA makes the group velocities independent of μ and T which also proves to be computationally advantageous as it removes dependence of the transport distribution function from temperature and doping. A single scan over a fixed transport distribution function can be used for the evaluation of the dependence of the transport coefficients on temperature and doping. The Fermi distribution function is solely responsible for the temperature and doping dependency of the transport coefficients.: E.g., only σ and κ_e dependent on τ are delivered by it [61]

2.2.4 AMSET

The AMSET code stands for ab initio scattering and transport method which uses the electronic Boltzmann transport equation (BTE) to calculate rates of scattering and mobilities using the Born approximation. The code takes into consideration of various scatterings like acoustic deformation potential (ADP), ionized impurity scattering (IMP), and polar optical phonon scattering (POP) which are the most common scattering types found in semiconductor-like materials. The ADP is responsible for the electron-phonon interactions. IMP represents the charge carriers scattering through the ionization of lattice, and POP includes the exchange of electrons and polar optical phonons. Matthiessen's rule can find out the resultant carrier relaxation time, the inverse of scattering rates by the following equation [62]:

$$\frac{1}{\tau} = \frac{1}{\tau_{ADP}} + \frac{1}{\tau_{IMP}} + \frac{1}{\tau_{POP}} \quad (17)$$

Where τ_{ADP} , τ_{POP} , τ_{IMP} are the time of relaxation from the ADP, POP and IMP scattering. In ADP and IMP scatterings, electrons undergo elastic scattering, where they neither gain nor lose energy. On the other hand, POP scatterings show inelastic scattering behaviour characterized by phonon emission or absorption-induced energy changes. The Fermi golden rule is applied to compute both elastic and inelastic scattering rates. This rule allows us to calculate the transition rates from an initial quantum state $n\mathbf{k}$ to a quantum state $m\mathbf{k} + \mathbf{q}$.

$$\tilde{\tau}_{nk \rightarrow mk+q}^{-1} = \frac{2\pi}{\hbar} |g_{nm}(k, q)|^2 \delta(\varepsilon_{nk} - \varepsilon_{mk+q}) \quad (18)$$

\hbar stands for Planck's constant, δ represents a Dirac delta function, and n relates to the Bose-Einstein distribution. The quantity ε_{nk} pertains to the energy of the state $|n\mathbf{k}\rangle$, while $g_{nm}(k, q)$ signifies the coupling matrix element governing the specific scattering process under consideration. To attain the scattering rates, it is necessary to have deformation, static and high-frequency constants along with elastic constants and dense and uniform band structures.



Figure 7: The Logo of AMSET

CHAPTER 3

RESULTS AND DISCUSSION

3.1 Structural Properties

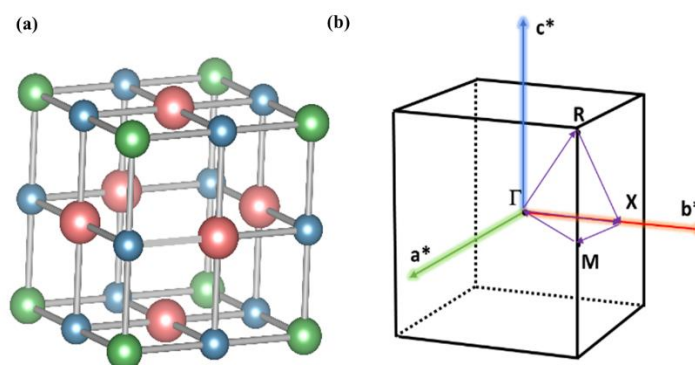


Fig 8. (a) Unit crystal structure (Blue, Green, and orange colour represent Ca, As, and Br atoms, respectively) (b) Brillouin zone of Ca_3AsBr_3

Ca_3AsBr_3 crystallizes in the cubic $Pm\bar{3}m$ space group (221) and the Wyckoff positions occupied by Ca atoms, As atoms, and Br atoms are $3c$ ($\frac{1}{2}, 0, 0$), $1a$ ($0, 0, 0$), and $3d$ ($0, \frac{1}{2}, \frac{1}{2}$), respectively as shown in Fig 8. Each As atom is surrounded by six Ca atoms, forming a corner-sharing octahedral with no tilting in these shared octahedra showing that they are perfectly aligned whereas each Br atom is bonded to four Ca atoms and these four Ca atoms are arranged in a square, flat (co-planar) [43]. We have performed structural optimization of this compound and fitted the Birch-Murnaghan equation of state to compute its equilibrium lattice parameters [44]. Table 1 lists the bond length and optimal structural characteristics. In the absence of strain, the lattice constant of Ca_3AsBr_3 is 5.96 \AA , this finding confirms the correctness and dependability of our computational methods by showing agreement with both experimental data and previously published theoretical predictions [29,30,45].

Table 1: The optimized lattice parameters (in Å), Volume of the unit cell (in Å³), and bond lengths (in Å) of Ca₃AsBr₃, along with available experimental data

System	a = b = c	Volume	Bond lengths	
			Ca-As	Ca-Br
Ca ₃ AsBr ₃	5.963 ^a , 5.92 ^b ,	212.07 ^a ,	2.97 ^a , 2.96 ^c ,	2.97 ^a , 2.96 ^c ,
	5.926 ^c , 5.95 ^d	210.64 ^d	2.98 ^d	2.98 ^d

^aPresent work, Others work: ^b[29], ^c[45], ^d[30]

3.2 Computational details

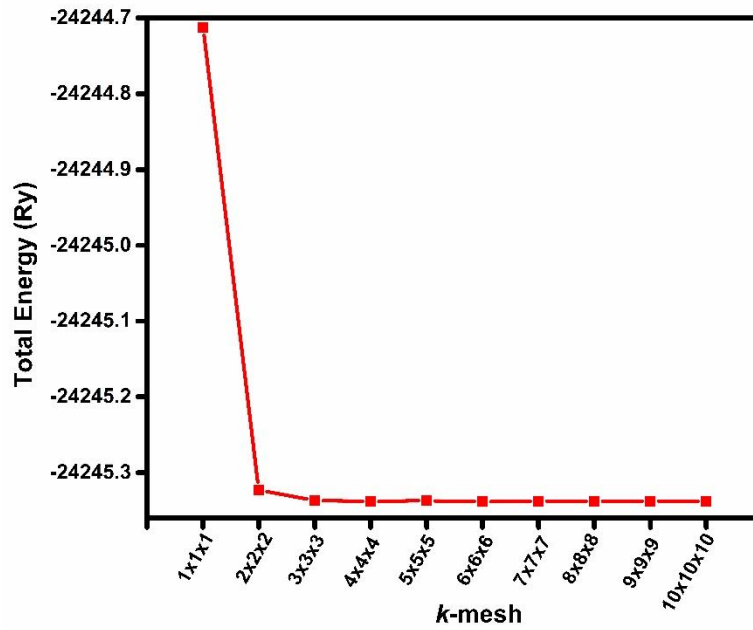


Fig. 9: Plot for the ground state energy with respect to the k -mesh varied in x -, y -, and z -directions by keeping $k_x = k_y = k_z$.

The full potential linearized augmented plane wave (FP-LAPW) method, which is implemented in WIEN2K software, was used to perform the structural, elastic, electrical, and TE characteristics of Ca₃AsBr₃ within the framework of DFT [34,35]. The generalized gradient approximation (GGA) of Perdew-Burke-Ernzerhof (PBE)

was used to optimize the structure [36]. We employed an optimized $10 \times 10 \times 10$ k -point mesh (Fig. S9) that produced 1000 k -points in the Brillouin zone, for the self-consistent calculations. The cut-off energies of the core and valence states were set to -6 Ry, and the plane wave cut-off was set as $RMT \times k_{max} = 7$. With an energy convergence of 0.000001 Ry, the Kohn–Sham equations were solved self-consistently. We used the Tran-Blaha modified Becke-Johnson (TB-mBJ) approach to determine the electronic band structure more accurately as most of the time GGA underestimates the band gaps of semiconductors [37]. It is a semi-local approximation to an atomic exact-exchange potential and a screening term. We used a mixing factor of 0.2 in the self-consistent calculations to ensure efficient convergence. For the density of states (DOS) calculations, we used a dense k -mesh of $25 \times 25 \times 25$. The Boltzmann Transport Equation (BTE) was solved under the rigid band approximation (RBA) and constant relaxation time approximation (CRTA), as implemented in the BoltzTraP2 code, in order to determine the TE characteristics [38]. For Vienna *Ab-initio* Simulation Package (VASP) calculations, we set the cutoff energy for plane wave basis functions at 520 eV, and a width of 0.01 eV for Gaussian smearing was used. To ensure accuracy, a strict convergence criterion for energy was fixed to 1×10^{-7} eV for the self-consistent calculations. Using the AMSET code interfaced with the VASP, we computed scattering rates and mobilities within the Born approximation by solving the electronic BTE in the momentum relaxation-time approximation [39,40]. Instead of using CRTA, this code estimates the relaxation time (τ) based on the number of distinct bands and k -point dependent scattering approaches. We computed scattering rates in this work by taking into account the following: (a) acoustic deformation potential (ADP), which is in charge of the phonon-electron coupling; (b) ionized impurity (IMP) scattering that denotes the scattering of charge carriers by ionization of the lattice; and (c) polar optical phonon (POP) scattering, which takes into account the interaction among polar optical phonons and electrons. We used Matthiessen's rule to determine the resulting carrier τ , which is the inverse of the scattering rate: $\frac{1}{\tau} = \frac{1}{\tau^{ADP}} + \frac{1}{\tau^{IMP}} + \frac{1}{\tau^{POP}}$, where τ^{ADP} , τ^{IMP} , and τ^{POP} are the relaxation times received from the ADP, IMP, and POP scattering, respectively [41]. Contrary to POP scatterings, which show inelastic scattering, ADP and IMP scatterings show elastic scattering, where electrons do not

gain or lose energy. DFT and density functional perturbation theory (DFPT) were used to calculate the parameters to produce the scattering rates, including polar-phonon frequency, elastic constants, wave-function coefficients, static and high-frequency dielectric constants, potentials, and dense and uniform band structures. An interpolation factor of 50 is used to predict τ and carrier mobility. The finite displacement approach was used to calculate the phonon dispersion of material to verify the dynamical stability, by building a $2 \times 2 \times 2$ supercell and using a $4 \times 4 \times 4$ k -point mesh using the Phonopy code [42]. Using the same supercell, we calculated anharmonic third-order interatomic force constants to obtain the lattice thermal conductivity using Phono3py [42] interfaced with VASP [39]. To obtain the lattice thermal conductivity and other related phonon properties such phonon density of states, phonon group velocity, Gruneisen parameter, and phonon lifetime we used a converged q -mesh of $25 \times 25 \times 25$ to sample the Brillouin zone.

3.3 Stability analysis

3.3.1 Thermodynamic stability

The thermodynamical stability of the compound is assessed through the calculation of the formation energy E_{for} using the following relation [46]:

$$E_{for} = \frac{[E_{Ca_3AsBr_3} - (3E_{Ca} - E_{As} - 3E_{Br})]}{N} \quad (a)$$

where N is the total number of atoms in the unit cell and $E_{Ca_3AsBr_3}$ is the ground state energy of Ca_3AsBr_3 , E_{Ca} , E_{As} , and E_{Br} are the total energy per atom for Ca, As, and Br in bulk form, respectively. The calculated E_{for} is determined to be -0.14 eV/atom, showing that the compound is thermodynamically stable.

3.3.2 Mechanical Stability

For a cubic system, the mechanical stability is usually analyzed by elastic constants of the material through Born stability criteria: $C_{11} > 0$, $C_{44} > 0$, $C_{11} - C_{12} > 0$, $C_{11} + 2C_{12} > 0$ [47]. The elastic constants calculated for considered unstrained and strained structures along with other mechanical parameters are mentioned in Table 2. Both unstained and

strained Ca_3AsBr_3 are found to satisfy the Born stability criteria and hence are mechanically stable.

Table 2: The elastic constants C_{11} , C_{12} , and C_{33} are in GPa, G_v , G_r , G_h , E , and B are in GPa, Poisson's ratio, Pugh's ratio, and A are dimensionless and melting temperature (K) corresponding to all compressive and tensile strains (in %)

Strain (%) \rightarrow	-3.00	-2.00	-1.00	0.00	1.00	2.00	3.00
Elastic Properties \downarrow							
C_{11}	116.53	115.17	106.05	71.58	62.49	53.47	36.36
C_{12}	13.70	7.31	5.42	15.20	13.75	14.24	17.28
C_{44}	21.26	30.69	28.59	15.37	13.49	10.84	9.16
Voigt Shear Modulus (G_v)	33.32	39.99	37.28	20.50	17.84	14.35	9.31
Reuss Shear Modulus (G_r)	27.77	37.08	34.56	18.79	16.43	13.21	9.31
Hill Shear Modulus (G_h)	30.55	38.54	35.92	19.64	17.13	13.78	9.31
Young's Modulus (E)	75.59	89.14	82.43	49.41	43.18	35.39	24.69
Poisson's Ratio (ν)	0.24	0.16	0.15	0.26	0.26	0.28	0.33
Bulk modulus (B)	47.98	43.26	38.96	33.99	30.00	27.31	23.64
Anisotropy Factor (A)	0.41	0.57	0.57	0.55	0.55	0.55	0.96
Pugh's Ratio (B/G)	1.57	1.12	1.08	1.73	1.75	1.98	2.54
Melting Temperature	1241.72	1233.68	1179.74	976.02	922.33	868.99	767.87

The bulk modulus (B) is obtained by $B=(C_{11}+2C_{12})/3$ and it decreases from 33.99 GPa for the unstrained structure to 23.64 GPa for 3% strain, whereas for 3% compressive strain it increases to 47.98 GPa. The shear modulus (G_h) is calculated based on the

Voigt, Reuss, and Hill approximations, and is given by the relation $G_h=(G_v+G_r)/2$, where $G_v=(C_{11}-C_{12}+3C_{44})/5$ and $G_r=(5(C_{11}-C_{12}) C_{44})/(4C_{44}+3(C_{11}-C_{12}))$ [48]. The Young's modulus (E) determined by $E=9BG_h/(3B+G_h)$, decreases sharply with strain, i.e., from 75.59 GPa at -3% to 24.69 GPa at $+3\%$. The Poisson's ratio (ν) is represented as $\nu=(3B-2G_h)/2(3B+G_h)$ its value rises from 0.26 for unstrained material to 0.33 for $+3\%$ strain indicating more lateral expansion upon axial compression with strain. Pugh's ratio (B/G) categorizes materials as brittle ($B/G<1.75$) or ductile ($B/G>1.75$) and this ratio increased with strain from 1.57 at -3% to 2.54 at $+3\%$, indicating a variation from a slightly brittle nature of compressive strains to highly ductile behavior under tensile strains. This ductility is advantageous for TE applications, as it enhances the ability of the material to withstand thermal and mechanical pressures during practical use. The anisotropy factor (A) is the degree of mechanical anisotropy in the material and it is found to be 0.41 at -3% strain and 0.96 at $+3\%$. We have also calculated the melting temperature for different strains as mentioned in Table 2. It is estimated using the empirical relation: $T_m = 553 \text{ K}+(5.91/\text{GPa}) C_{11} \pm 300 \text{ K}$, T_m decreases with increasing strain, indicating reduced thermal stability. The experimental value shows that deformation of the Ca_3AsBr_3 compound does not happen till 920 K [45], which verifies its stability. The value of calculated mechanical parameters are in good comparison to previously reported data [30].

3.3.3 Dynamical stability

We have also analyzed the dynamical stability of the Ca_3AsBr_3 compound at ambient (Fig. 10a) and for 3% compressive and tensile strain (Fig. 10c and 10d) by obtaining phonon dispersion along with Γ -X-M- Γ -R-X direction in the Brillouin zone (shown in Fig. 8b), calculated using finite displacement approach. The absence of the negative frequencies in the phonon dispersion validates the dynamical stability of the cubic phase of Ca_3AsBr_3 at ambient and under applied strain. The unit cell has 7 atoms, so there are 21 total phonon branches, i.e., 3 acoustic and 18 optical phonon modes in the phonon dispersion curve. Higher branches of the dispersion spectra indicate the optical branches that correlate to the frequency range of 2–8 THz, while the lower

branches correspond to the acoustic branches with the corresponding frequency range of 0–2 THz. It can be observed that the phonon dispersion becomes narrower with the increase in tensile strain, which might lead to enhanced phonon scattering and low phonon group velocity, consequently, the reduced lattice thermal conductivity,

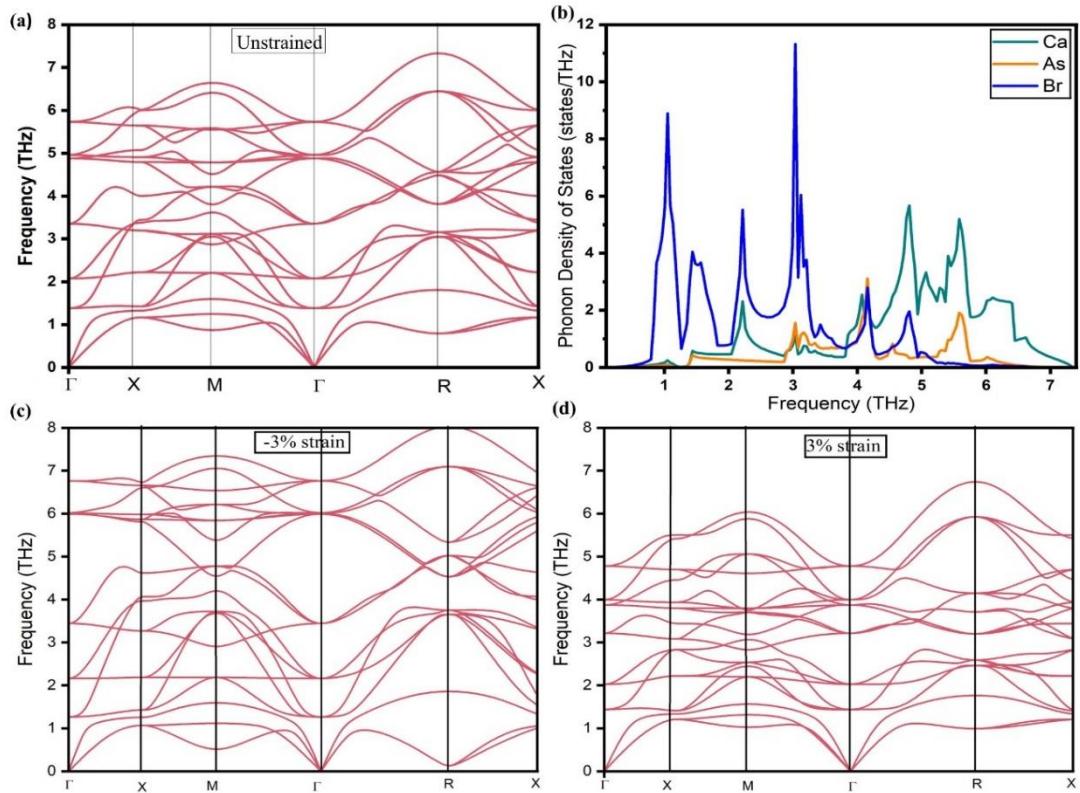


Fig. 10: **(a)** The phonon dispersion curve of unstrained Ca_3AsBr_3 and **(b)** Phonon Density of states **(c)** phonon dispersion curve of Ca_3AsBr_3 under strain -3% **(d)** phonon dispersion curve of Ca_3AsBr_3 under strains $+3\%$

compared to the unstrained structure. On the other hand, the opposite trend is observed with the increase in compressive strain. Additionally, the phonon density of states (PDOS) as shown in Fig. 10 (b), is determined to examine the atomic contributions to the acoustic and optical modes. The acoustic and low-frequency lying optical modes are mainly contributed by the vibrations of Br atoms with a negligible contribution of Ca and As atoms. The high-frequency optical modes are dominated by the vibrations of Ca atoms and the substantial contribution of As and Br atoms. There is no band gap

between acoustic and low-frequency optical modes, which might enhance phonon scattering and lead to low lattice thermal conductivity [49].

3.4 Electronic Properties

Table 3: Bandgaps for different strains

Strain (%)	Band Gap in (eV)			
	GGA (without SOC)	GGA (with SOC)	TB-mBJ (without SOC)	TB-mBJ (with SOC)
-3	1.559	1.480	2.275	2.205
-2	1.642	1.564	2.356	2.287
-1	1.664	1.587	2.364	2.296
0	1.729	1.654	2.425	2.385
1	1.744	1.670	2.440	2.374
2	1.796	1.796	2.493	2.428
3	1.842	1.842	2.541	2.447

The electronic band structures of both unstrained and strained material with and without SOC effect were calculated using both GGA and TB-mBJ to understand the electronic properties of Ca_3AsBr_3 . The band gap values obtained using these functionals with and without SOC are presented in Table 3, corresponding to all considered structures.

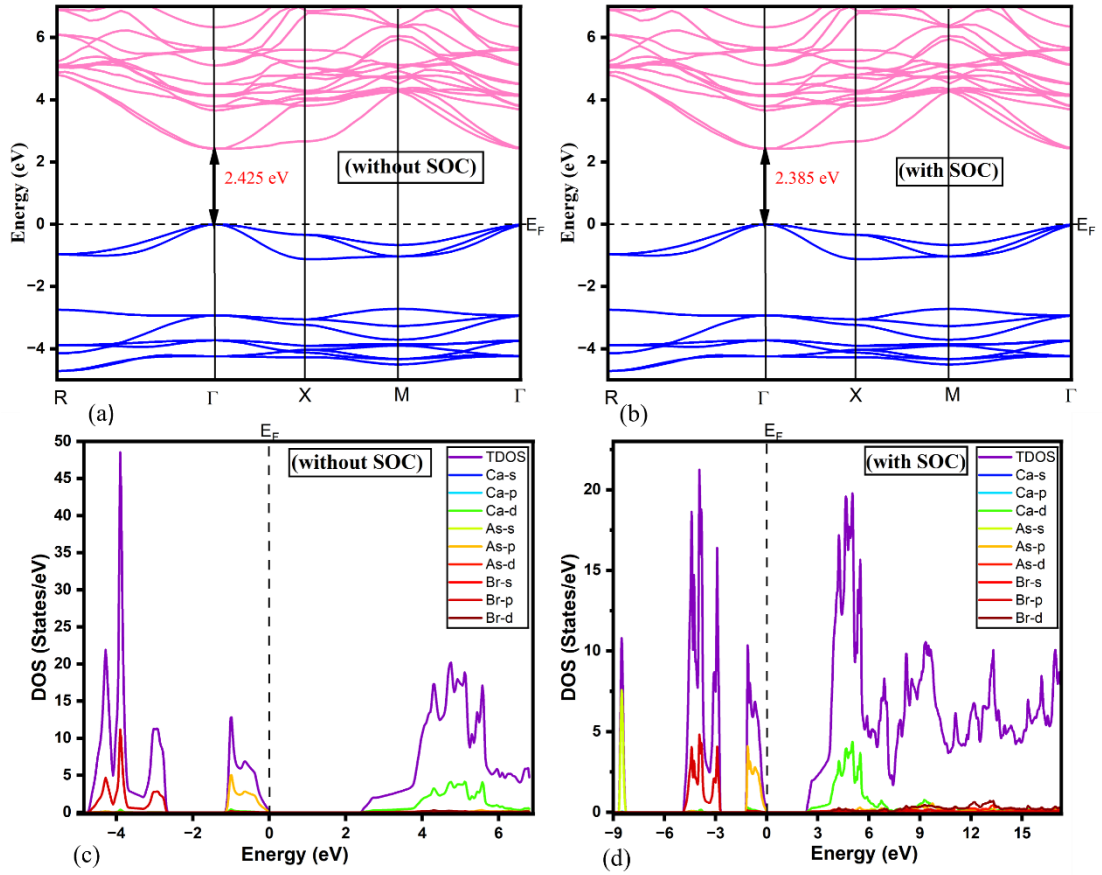


Fig. 11: Electronic band structures and density of states of unstrained Ca_3AsBr_3 with and without SOC

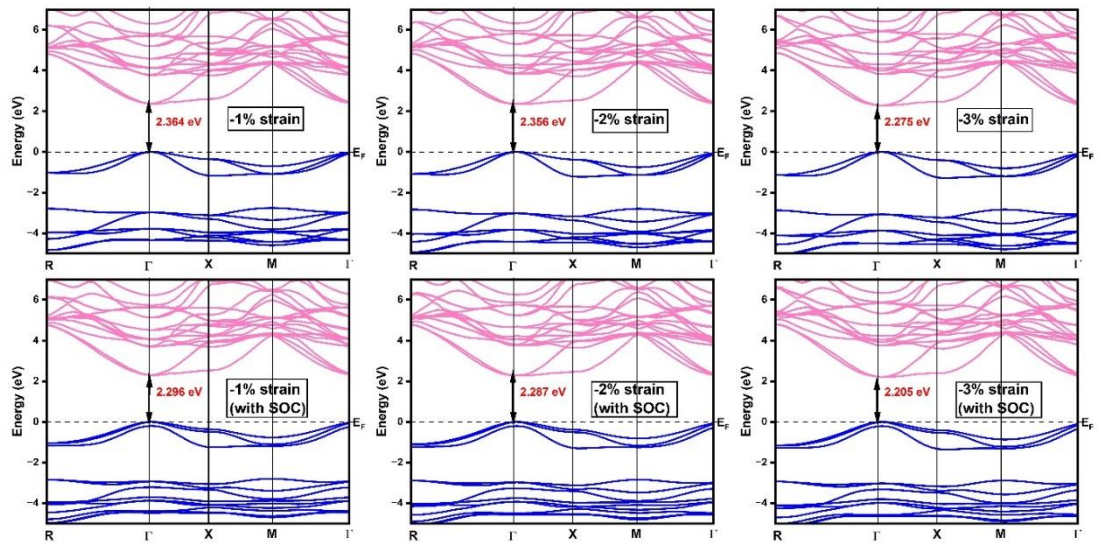


Fig. 12: Electronic band structures of Ca_3AsBr_3 with (upper panel) and without SOC (lower panel) under compressive strains

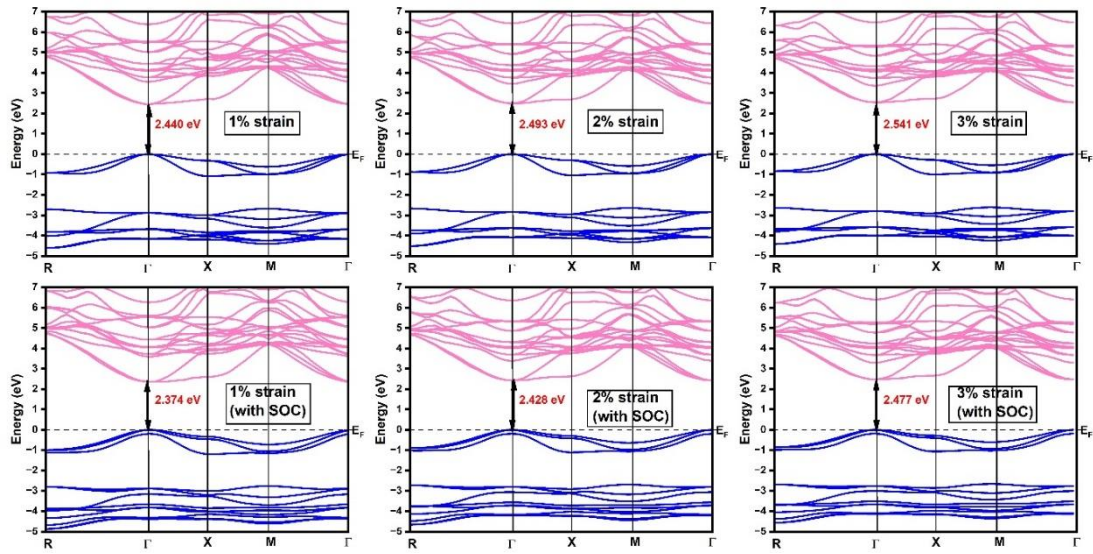


Fig. 13: Electronic band structures of Ca_3AsBr_3 with (upper panel) and without SOC (lower panel) under tensile strain

The band gap value of unstrained Ca_3AsBr_3 calculated using GGA-PBE is 1.65, which is in good agreement with the previously reported value of 1.63 by Islam et al. [30]. The electronic band structure of Ca_3AsBr_3 with 0% strain along the high symmetry path ($\text{R}-\Gamma-\text{X}-\text{M}-\Gamma$) in the Brillouin zone is shown in Fig. 11. Also, the band structures for both compressive and tensile strains with and without SOC are shown in Fig 12 and Fig 13. The Fermi energy level was taken at 0 eV to make it simpler to determine the bandgap. The band structure for this system revealed that it is a semiconductor with a direct bandgap and remains direct under the impact of all strains. Also, from the electronic structure, it is observed that the bandgap decreases and increases with the increase in the compressive and tensile strain, respectively, which might result in enhanced ZT for the strained structures. On comparing the dispersion curves of +3% and -3%, we obtained more dispersive valence and conduction bands in the vicinity of the Fermi level for the -3% strain, while more flattened bands are obtained for the +3%. It means a large Seebeck coefficient and enhanced electronic density of states can be observed for tensile strain, and a high carrier mobility and high electrical conductivity for the compressive strain for both types of charge carriers. Further, analysis of the band structure shows that the material has triply degenerate states at Γ -point. This degeneracy affects the TE performance by impacting important parameters

such as S , σ , etc. The density of states (DOS) was obtained to get deeper insights about the electronic characteristics of the material, as shown bottom panel in Fig. 11. The high effective DOS near the Fermi level, contributed by the triply degenerate bands, increases the number of accessible states for charge carriers also leading to higher S . The degeneracy also provides multiple paths for carrier transport, reducing scattering and thereby improving the carrier mobility (μ), which directly increases the σ of the material. The balance between carrier concentration and S is also maintained by this triply degenerate bands, which enhances power factor, which affects ZT in a good way. The p and d orbitals of As atoms contribute most to the valence band (VB), whereas the d -orbital of Ca atoms contribute most to the conduction band (CB). The VB maxima show sharp peaks, suggesting the possibility of a high S . The 2 eV bandgap in DOS proves that it is ideal case for TE as it allows for selective carrier transport without excessive carrier excitation, maintaining a balance between σ and S .

3.5 Thermoelectric Properties

The TE properties of Ca_3AsBr_3 were analysed using the semi-classical BTE as implemented in the BoltzTraP2 code [38]. The semiclassical Boltzmann model under the CRTA and RBA for an anisotropic system was used to calculate the transport coefficients (S , σ , κ_e), and the relations used were:

$$S_{\alpha\beta}(\mu, T) = \frac{1}{eT\sigma_{\alpha\beta}(\mu, T)} \int \sigma_{\alpha\beta}(\varepsilon)(\varepsilon - \mu) \left(-\frac{\partial f(T, \varepsilon, \mu)}{\partial \varepsilon} \right) d\varepsilon \quad (\text{b})$$

$$\kappa_{\alpha\beta}^e(\mu, T) = \frac{1}{e^2 T \Omega} \int \sigma_{\alpha\beta}(\varepsilon)(\varepsilon - \mu)^2 \left(-\frac{\partial f(T, \varepsilon, \mu)}{\partial \varepsilon} \right) d\varepsilon \quad (\text{c})$$

$$\sigma_{\alpha\beta}(\mu, T) = \frac{1}{\Omega} \int \sigma_{\alpha\beta}(\varepsilon) \left(-\frac{\partial f(T, \varepsilon, \mu)}{\partial \varepsilon} \right) d\varepsilon \quad (\text{d})$$

where $f(T, \varepsilon, \mu)$ is the Fermi-Dirac function, e is the electron charge, Ω is the reciprocal space volume, $\sigma_{\alpha\beta}(\varepsilon)$ is the conductivity tensor, and ε is the carrier energy, which is expressed as:

$$\sigma_{\alpha\beta}(\varepsilon) = \frac{1}{N} \sum_{i,k} \sigma_{\alpha\beta}(i, k) \frac{\delta(\varepsilon - \varepsilon_{i,k})}{d\varepsilon} \quad (\text{e})$$

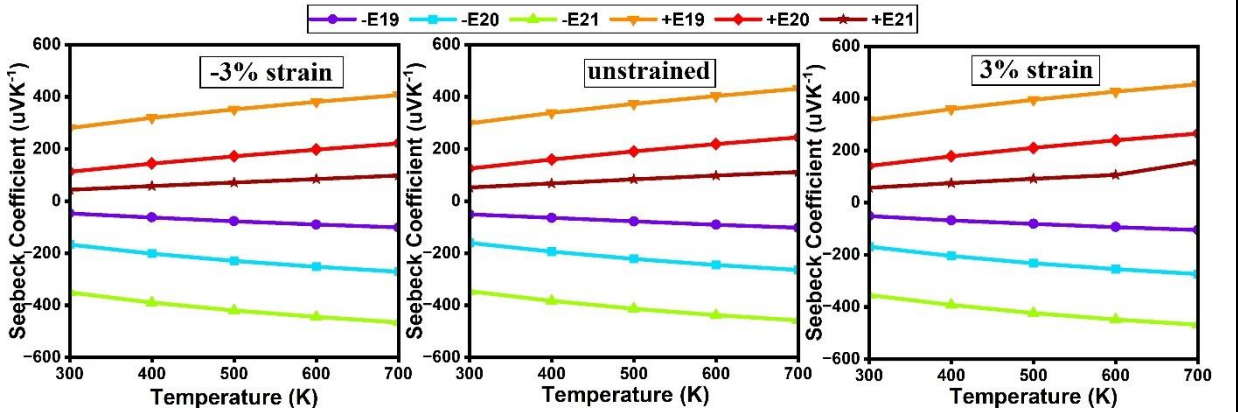
From equations (b-d) it can be inferred that the transport coefficients have strong dependence on the carrier concentration and temperature. A positive μ shows a rise in

the Fermi level during n -type doping. On the other hand, the Fermi level falls with p -type doping, resulting in a negative μ [50]. Therefore, for both p -type and n -type doping, we calculated S , σ , κ_e and associated PF and ZT as a function of temperature for charge carrier concentrations $\pm 10^{19} \text{ cm}^{-3}$, $\pm 10^{20} \text{ cm}^{-3}$, and $\pm 10^{21} \text{ cm}^{-3}$, and strains 0%, $\pm 1\%$, $\pm 2\%$, and $\pm 3\%$.

For degenerate semiconductors, S is expressed as [51]:

$$S = \frac{8\pi^2 k_B^2}{3eh^2} m^* T \left(\frac{\pi}{3n} \right)^{\frac{2}{3}} \quad (f)$$

where n is the charge carrier concentration, m^* is effective mass, and T is the absolute temperature. As shown in Fig. 14 for unstrained and $\pm 3\%$ strain, at fixed carrier concentration, for both p - and n -type S increased with an increase in temperature. S increases with temperature in semiconductors due to the increasing influence of thermally excited carriers. However, at fixed temperature S , it decreased with an increase in carrier concentration from $1 \times 10^{19} \text{ cm}^{-3}$ to $1 \times 10^{21} \text{ cm}^{-3}$ for both p - and n -type. S behaved in a similar way for $\pm 1\%$, $\pm 2\%$ strains. The maximum value observed of S for the unstrained structure is $-458.23 \mu\text{VK}^{-1}$ at 700 K, also it is -434.283 , -482.366 , -464.998 , -451.827 , -458.449 , and $-468.289 \mu\text{VK}^{-1}$ for -1 , -2 , -3 , $+1$, $+2$, and $+3\%$ strains, respectively, at 700 K for optimal carrier concentrations. A negative sign represents n -type semiconducting behaviour. The S goes as high as $482 \mu\text{V/K}$ at compressive strain, comparable to KInC_3 with S of $500 \mu\text{V/K}$ [52].



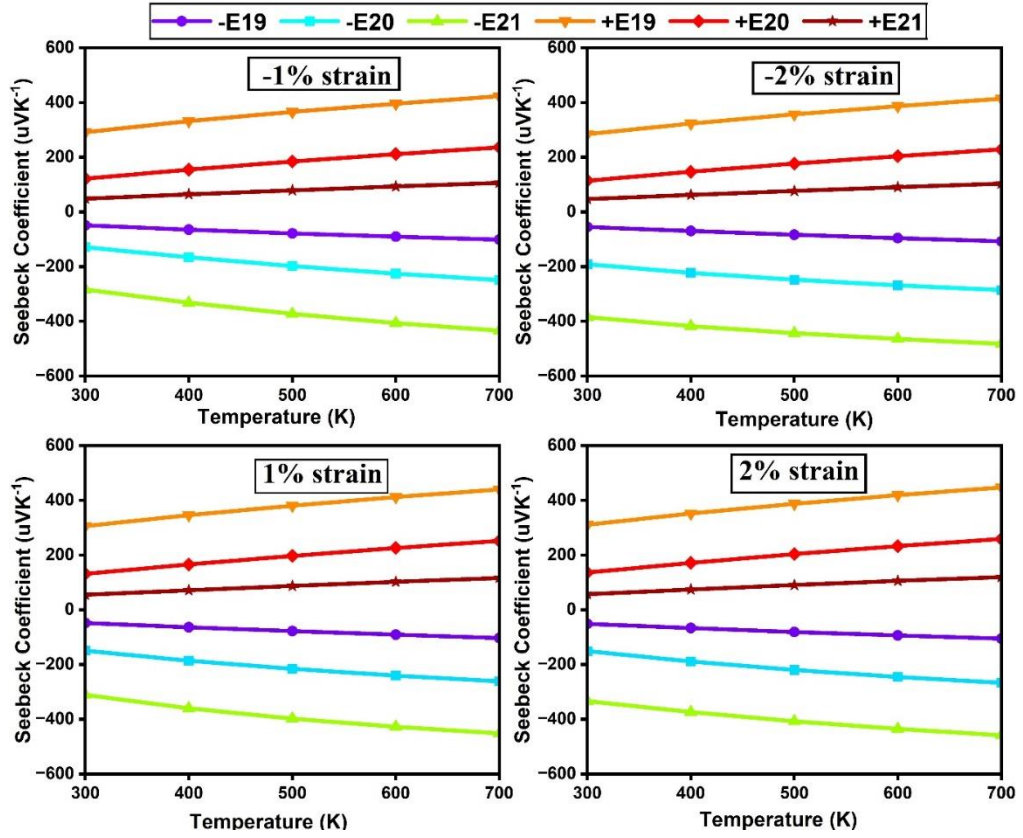


Fig. 14: Seebeck coefficient vs temperature for different carrier concentrations for different strains.

As Boltztrap2 provides σ/τ , κ_e/τ where τ is taken as constant value, so we used AMSET code to find exact carrier (hole/electron) relaxation time and overall mobility by assessing different scattering phenomena in system. We have taken into account the three fundamental carrier scattering rates (ADP, IMP, and POP). The upper panel of Fig. 15 displays the scattering rate across the temperature range (300–700 K), for unstrained material for $1 \times 10^{20} \text{ cm}^{-3}$ charge carrier concentration for both *n*- and *p*-type. It shows that the POP lifetimes are an order of magnitude larger than ADP and IMP scattering-based lifetimes which shows that POP scattering increased the overall lifespan value. The order of dominance for both conduction- and valence-band edges was $\text{POP} > \text{ADP} > \text{IMP}$ for all strains. Additionally, the lower panel in Fig. 15 shows the mobility of charge carriers at concentration $1 \times 10^{20} \text{ cm}^{-3}$ for 0% strained structure, it shows at 300 and 700 K, the values for the total mobility of electrons (holes) are approximately 12.97 (9.05) $\text{cm}^2\text{V}^{-1}\text{s}^{-1}$ and 5.51 (3.74) $\text{cm}^2\text{V}^{-1}\text{s}^{-1}$, respectively. The μ

of the electrons is comparatively greater than that of the holes, confirming that the material could effectively raise the ZT for n -doping. Furthermore, we see a drop in ADP, POP, and overall mobilities as the temperature rises, this can be explained by the increased quantity of phonons contributing to high scattering. Since temperature often has less of an effect on IMP scattering, their mobility is rather constant over the temperature ranges.

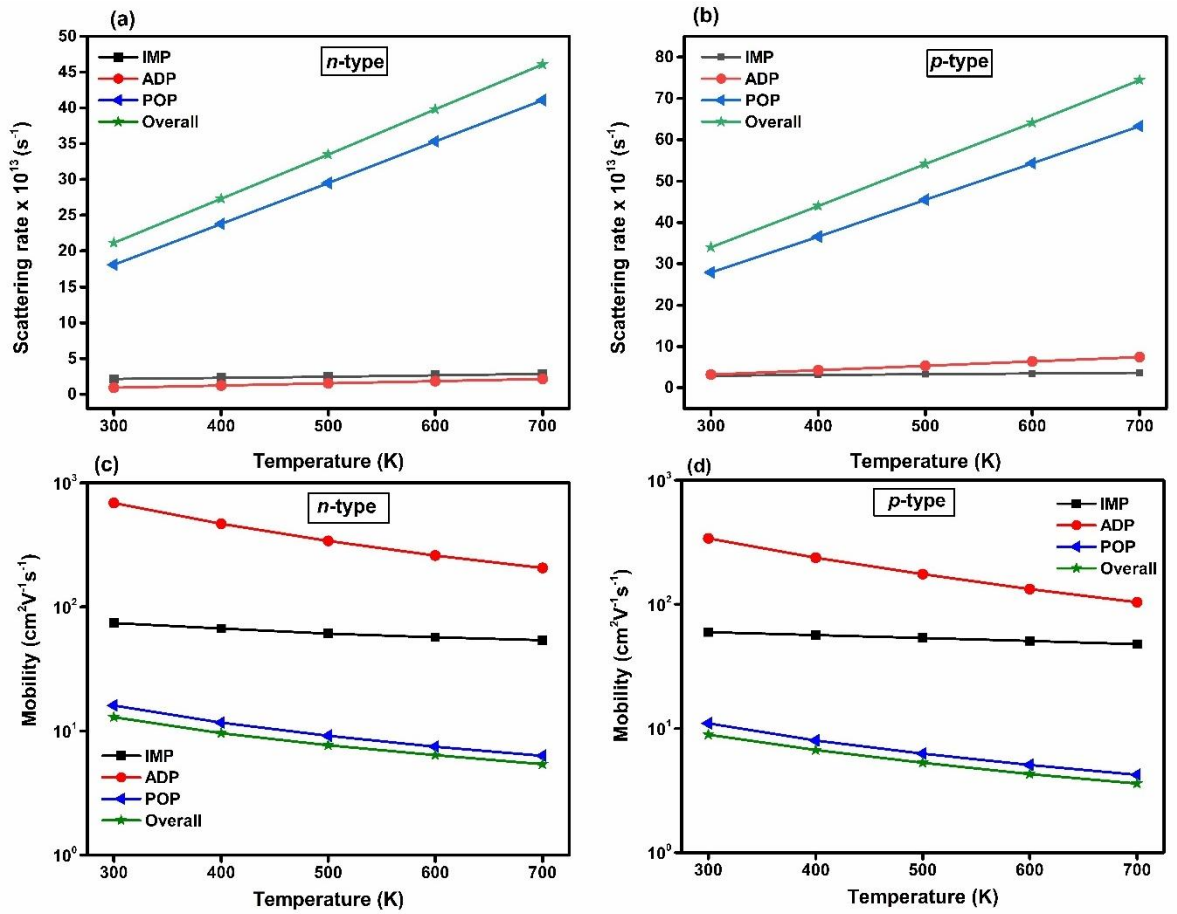


Fig. 15 Scattering rates and carrier mobility due to different scatterings by varying the carrier concentration of Ca_3AsBr_3 for both p -type and n -type

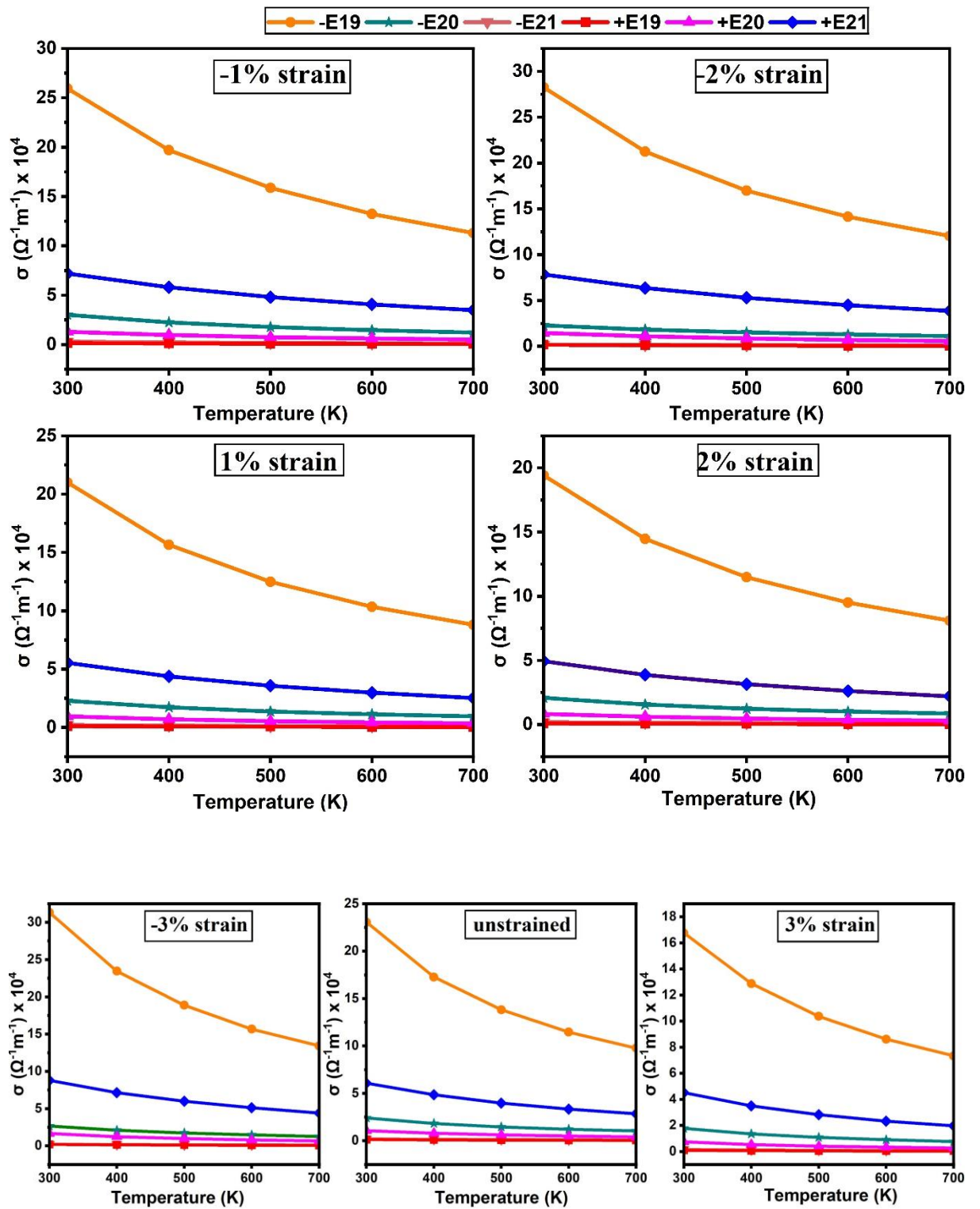


Fig. 16: Electrical conductivity vs temperature for different carrier concentrations for different strains 0%, $\pm 1\%$, $\pm 2\%$, and $\pm 3\%$

Fig. 16 illustrates that for 0%, ± 1 , $\pm 2\%$, and $\pm 3\%$ strains, σ reduces for almost all doping concentrations with temperature. The small electrical conductivity is obtained for the p -type in comparison to the n -type as a consequence of the flatter valence bands around the Fermi level. The minimum σ for each strain was shown by carrier concentration $1 \times 10^{19} \text{ cm}^{-3}$ for n -type doping with values 14.64, 16.20, 17.89, 13.28, 12.20, 11.32, and $9.42 \times 10^4 \Omega^{-1}\text{m}^{-1}$ for -1, -2, -3, 0, +1, +2, +3% strain, respectively. The minimum value of σ for p -type doping with hole concentration of $1 \times 10^{19} \text{ cm}^{-3}$ is 0.05, 0.06, 0.07, 0.04, 0.03, 0.03, and $0.02 \times 10^4 \Omega^{-1}\text{m}^{-1}$ for -1, -2, -3, 0, +1, +2, +3% strain, respectively. The reduced electrical conductivity for tensile strain can be attributed to strain-induced band structure modifications. i.e., less dispersive conduction and valence bands (as depicted in Fig. 11) that increase the effective mass of charge carriers and hence decrease their carrier mobilities. The behaviour is still temperature-dependent, and phonon scattering is the leading factor at high temperatures.

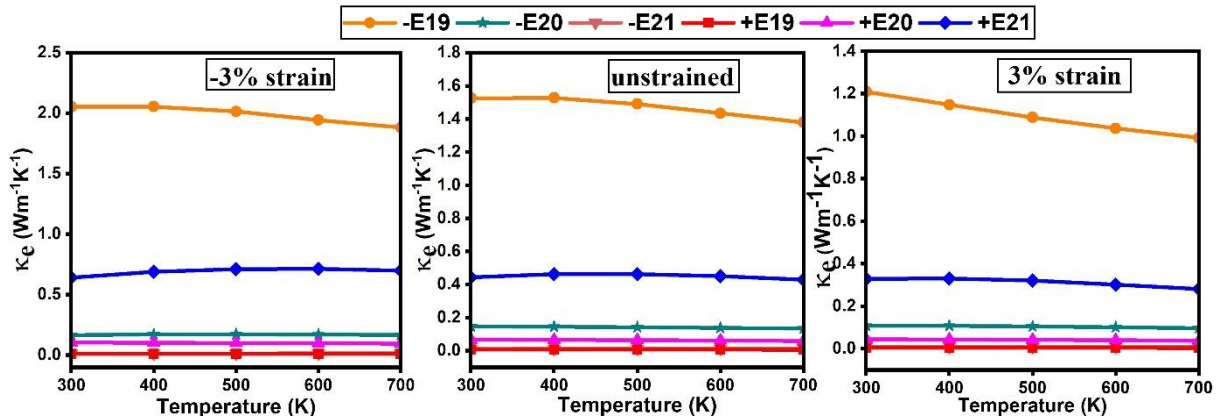


Fig. 17: Electronic thermal conductivity vs temperature for different carrier concentrations for different strains

The κ_e for 0%, ± 1 , $\pm 2\%$, and $\pm 3\%$ strains are displayed in Fig. 17. The highest values are shown by carrier concentration of $1 \times 10^{19} \text{ cm}^{-3}$ for n -type doping for each strain. This is an immediate consequence of their higher electrical conductivity as prescribed by the Wiedemann-Franz law which states that κ_e and σ are related by formula $\kappa_e = L \sigma T$ (where L is Lorentz number) [53]. The weak temperature dependence implies that electron-phonon scattering is of lesser importance for heat

transport in this regime. Furthermore, increased carrier concentrations map to greater κ_e , reinforcing the importance of charge carriers for electronic thermal conduction. This is important for TE performance because high κ_e tends to decrease the ZT .

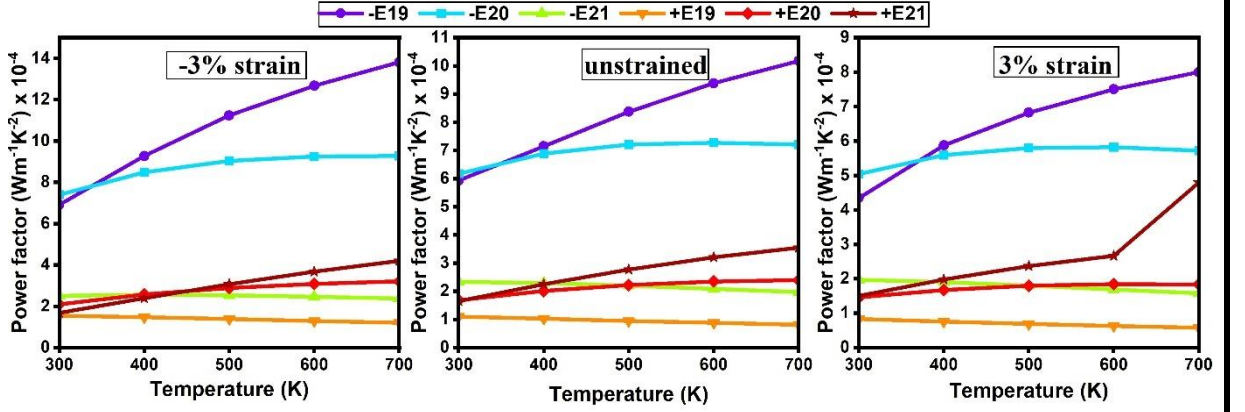


Fig. 18: Power factor vs temperature for different carrier concentrations for different strains.

The variation of PF for different temperatures at various doping concentrations is shown in Fig. 18 for 0 and $\pm 3\%$ strains. As charge carrier concentration increased from $1 \times 10^{19} \text{ cm}^{-3}$ to $1 \times 10^{21} \text{ cm}^{-3}$, PF decreased for n -type doping. It increased for all temperatures for all carrier concentrations and this behaviour can be analysed on basis of their S and σ as $PF = S^2 \sigma$. The maximum values for -1, -2, -3, 1, 0, 1, 2, and 3% strains, respectively, are 11.66×10^{-4} , 13.85×10^{-4} , 13.81×10^{-4} , 10.17×10^{-4} , 9.36×10^{-4} , 8.95×10^{-4} , and $8 \times 10^{-4} \text{ Wm}^{-1}\text{K}^{-2}$ at 700 K each. We obtained higher PF values for the n -type because of high carrier mobility and high electrical conductivity of the electron carriers, whilst the lower PF for the p -type, corresponding to all considered structures, and this behaviour is consistent with the electronic band structure (as shown in Fig. 11).

Using the single-mode relaxation-time approximation, κ_l was calculated as a summation of individual phonon modes λ contributions following the equation [54]:

$$\kappa_l = \frac{1}{NV} \sum_{\lambda} C_{\lambda} v_{\lambda} \otimes v_{\lambda} \tau_{\lambda} \quad (\text{g})$$

where V is the volume of the unit cell, and N is the number of phonons wavevectors, $v_\lambda \otimes v_\lambda$ are the tensor products of the group velocities, C_λ are the heat capacities and τ_λ are the lifetimes.

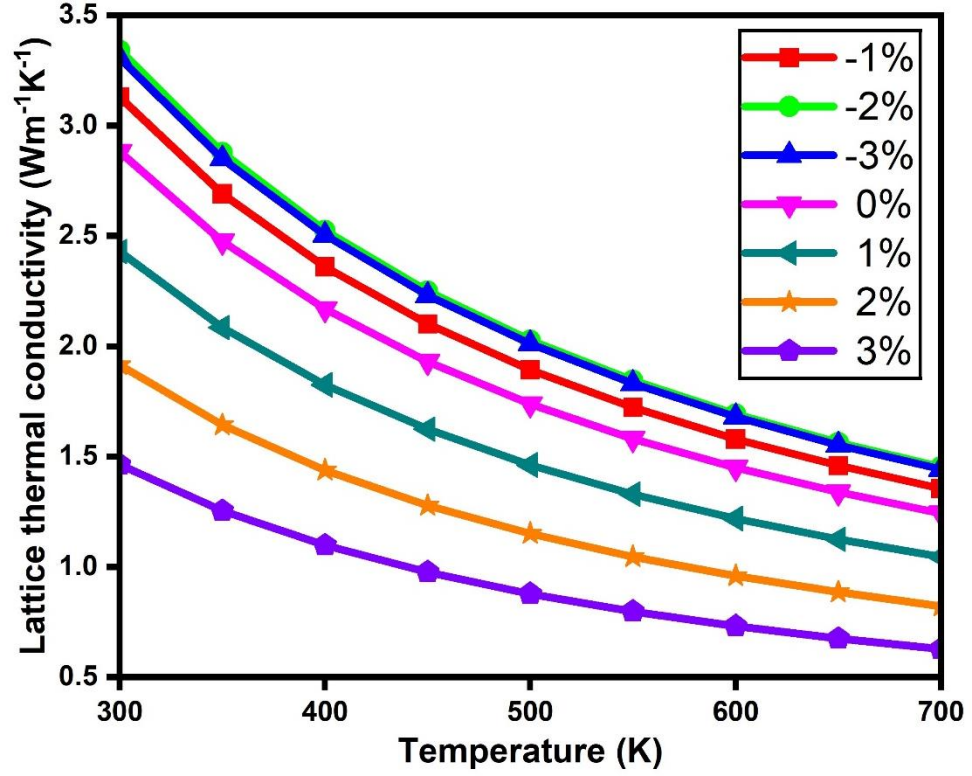


Fig.19: Lattice thermal conductivity for various strains at temperatures 300 to 700 K

Fig.19 shows the variation of κ_l for each strain with temperature. The value of κ_l estimated at room temperature is $2.88 \text{ Wm}^{-1}\text{K}^{-1}$ for unstrained structure, and it decreased to $1.24 \text{ Wm}^{-1}\text{K}^{-1}$ at 700 K temperature. For -1%, -2%, -3%, +1%, +2%, and +3% strains, the minimum value of κ_l is at 700 K i.e. 1.45, 1.44, 1.24, 1.04, 0.82, and $0.63 \text{ Wm}^{-1}\text{K}^{-1}$, respectively. This reduction in κ_l is advantageous for enhancing the high TE conversion efficiency of the material. Finally, κ is obtained by adding κ_e and κ_l . The calculated value of κ is $0.72 \text{ Wm}^{-1}\text{K}^{-1}$ at 700 K temperature for n -type doping concentration of 10^{20} cm^{-3} for 3% tensile strain.

To gain a deeper understanding of the lattice dynamics that causes a significant strain-induced change in κ_l , we analyzed the group velocity, phonon lifetime, and Gruniesen

parameter for Ca_3AsBr_3 as a function of frequency, as displayed in Fig. 20. The phonon v_g was obtained from the phonon dispersion relations, which were calculated using force constants within harmonic approximation. As expected, and illustrated in Fig. 20(a)–(c) for -3%, 0%, and 3% strains, the strain in these systems has a substantial influence on both the v_g of phonons and hence the thermal transport of phonons. Consequently, when the tensile/compressive strain increases, the v_g of phonons are noticeably reduced/increased. Increasing tensile strain results in narrower dispersions for phonon modes, which is depicted in Fig. 10, and weaker bonds. To characterize the values of v_g quantitatively for each strain, the average v_g over the phonon modes is evaluated. The average v_g of Ca_3AsBr_3 for -3%, -2%, -1%, 0%, 1%, 2%, and 3%, respectively, comes out to 1.31, 1.21, 1.12, 1.04, 0.97, 0.92, and 0.89 (kms^{-1}). Fig 20(d)–(f) shows the mode Grüneisen parameter (γ) for unstrained and $\pm 3\%$. The average value of γ for unstrained Ca_3AsBr_3 is 1.25 while on increasing the strain, the average γ rises from 0.57 to 1.68 for -3% to +3% strained structure, indicating enhanced lattice anharmonicity in the case of tensile strain. A higher γ implies stronger phonon–phonon scattering, which directly contributes to the observed reduction in phonon lifetime and thermal conductivity. Then, we considered the phonon lifetime to analyse the phonon-phonon scattering, as shown in Fig. 20(g)–(i) for 0 and $\pm 3\%$ strain at 300 K. It exhibits a consistent trend, a significant rise in phonon scattering is observed as the strain increases. Also, based on the distribution of phonon lifetimes, it is evident that the primary factor influencing κ_l is the acoustic branches, whereas the optical mode has a lesser impact. For all structures at a low frequency, we can see phonon lifetime reaches up to 30 ps. At mid to high frequencies, phonon lifetimes are shorter and clustered to a few picoseconds, indicating higher scattering. Therefore, the combined effects of reduced group velocity, shortened phonon lifetime, and increased

anharmonicity with tensile strain comprehensively explain the decreased lattice thermal conductivity in strained Ca_3AsBr_3 .

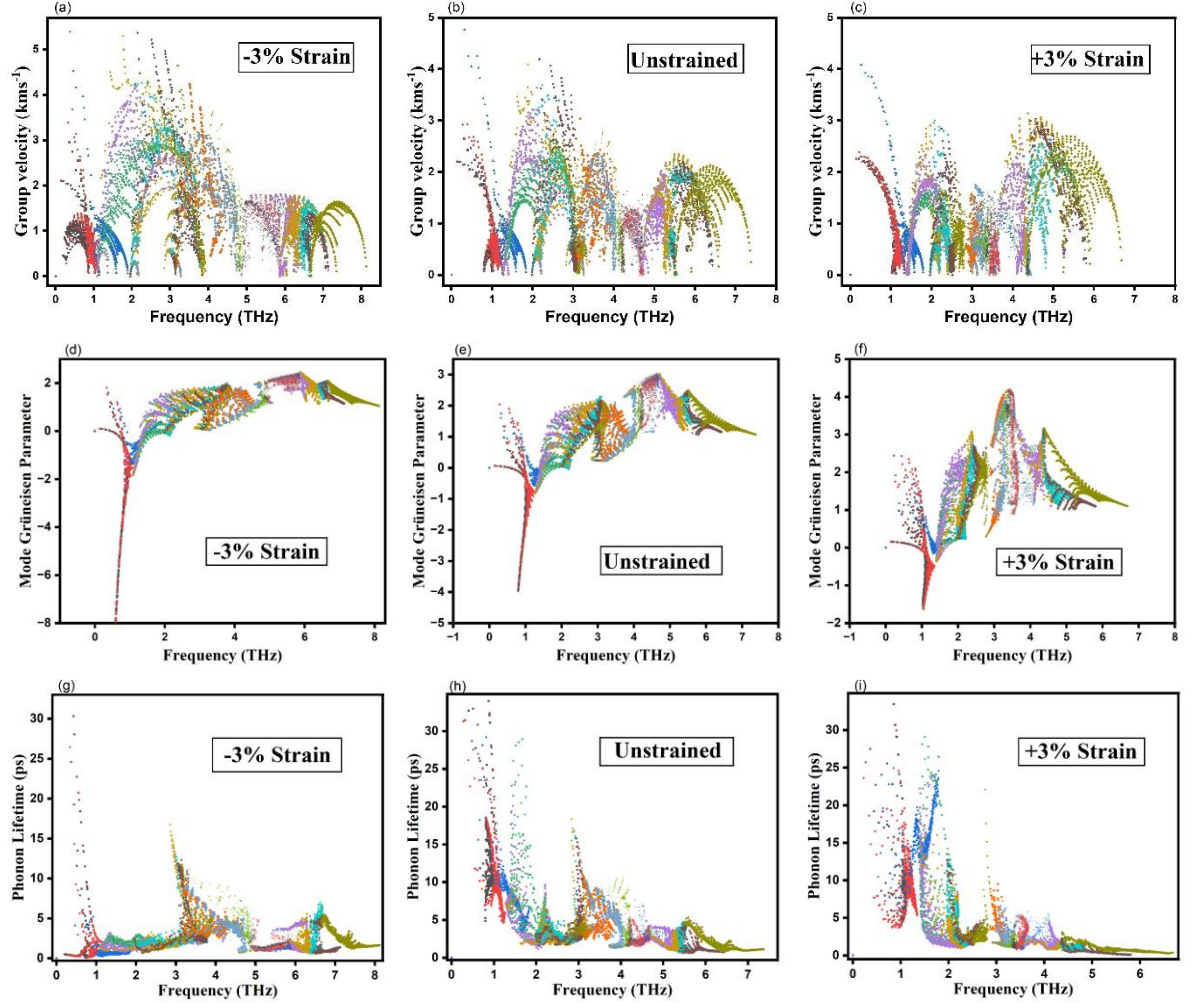


Fig. 20 (a-c) Phonon group velocity, (d-f) Mode Grüneisen parameter (g-i) phonon lifetime corresponding to all phonon modes as a function of frequency for the unstrained and $\pm 3\%$ strained Ca_3AsBr_3 .

The TE figure of merit (ZT) is a significant parameter used to evaluate the efficiency of a material for power generation from heat. The higher the value of ZT , better the TE efficiency, and thus by determining it, the influence of strain, doping and temperature on the TE performance of material were analysed.

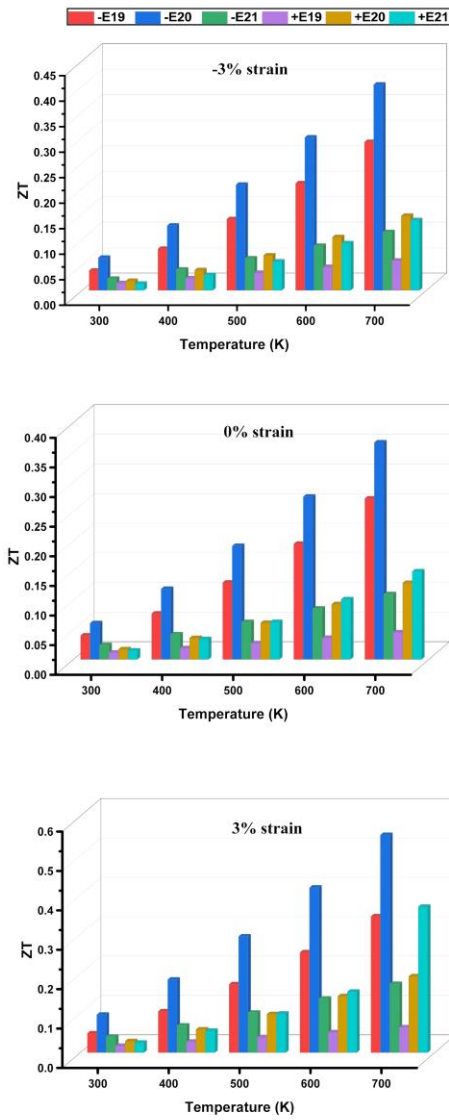


Fig. 21 ZT value for various strains for 300-700 K temperature for fixed carrier concentrations for 0%, +3%, -3% strains.

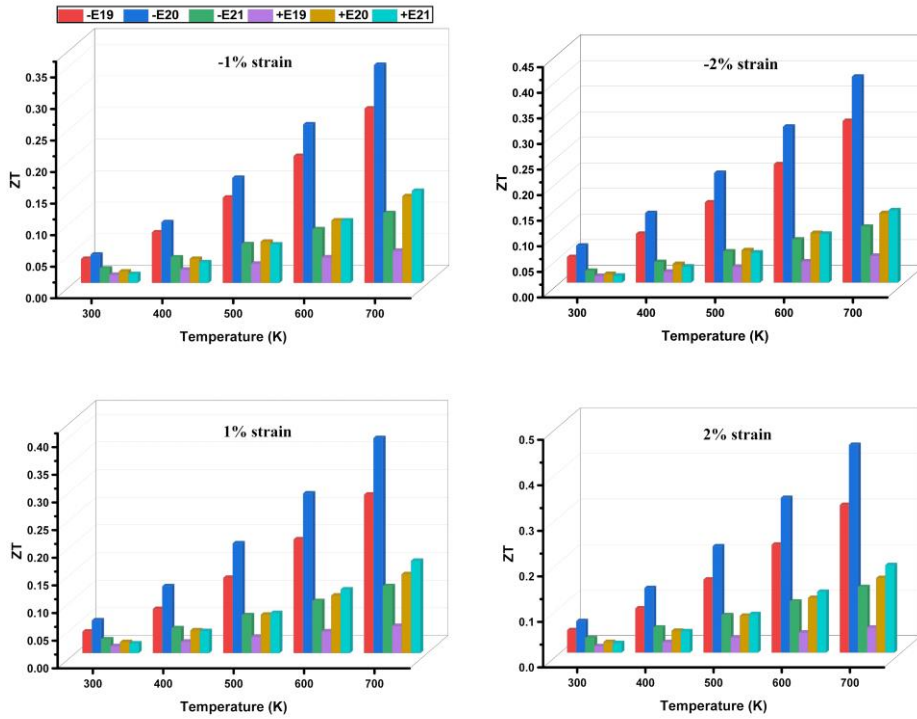


Fig. 22: ZT value for various concentrations for 300-700 K temperature for different carrier strains $\pm 1\%$ and $\pm 2\%$

Fig. 21 shows that for 0 and $\pm 3\%$ strain for each temperature ZT is highest at 1×10^{20} cm^{-3} for n -type doping, a similar trend is followed by ± 1 and $\pm 2\%$ strains as shown in Fig. 22. The maximum values for -1, -2, -3, 0, 1, 2, and 3 % strains are 0.34, 0.4, 0.4, 0.36, 0.38, 0.45, and 0.55, respectively at 700 K. Temperature and charge carrier concentration have an impact on the ZT value. The relationship between the S and carrier concentration is inverse for both electrical and thermal conductivity. As a result, it is not simply an assumption that raising the carrier concentration will result in a higher ZT value. This is due to the fact that while the σ and κ_e both rise with increasing carrier concentration, the S falls. Overall, these coupled parameters are optimized in such a way that ZT is maximized. Our research revealed strained Ca_3AsBr_3 with a peak ZT of 0.55 at 700 K, being as high as of double perovskite $\text{Cs}_2\text{AuYCl}_6$ [55]. These findings indicate that strain engineering in Ca_3AsBr_3 can efficiently improve TE performance.

CONCLUSIONS AND FUTURE SCOPE

In this study, we have examined the thermoelectric properties of halide perovskite Ca_3AsBr_3 for various strains at different temperatures for different carrier concentrations using density functional theory and the Boltzmann transport equation. The obtained structural parameters aligned well with the available experimental and theoretical values. We have verified mechanical, thermodynamic, and dynamical stability by calculating elastic constants, formation energy, and analysing the phonon dispersion relations, respectively. The electronic band structures showed that it is a semiconductor with a direct bandgap, and remains direct even with the compressive and tensile strain. The strain modified the electronic band structure and improved the mobility of the charge carrier and hence the PF . We found that isotropic tensile strain significantly reduces lattice thermal conductivity (κ_l) by decreasing phonon group velocities, shortening phonon lifetimes, and enhancing anharmonicity, as reflected in the Grüneisen parameter. For 3% strain, a κ_l is found as $0.63 \text{ Wm}^{-1}\text{K}^{-1}$ and a peak value of ZT , i.e., 0.55, is obtained at 700 K for the n -type doping concentration of 10^{20} cm^{-3} . The ZT can be further enhanced by decreasing the bandgap by introducing vacancies or interstitials that can create defects, or by doping of some alloy or other element that can introduce more energy states or by further varying carrier concentration. Also, material can be nanostructured, which can not only reduce the bandgap but also reduce lattice thermal conductivity. The electron and hole carrier concentrations explored in the present work are limited to a few discrete values, finer carrier concentration tuning further leads to improved PF and ZT . The specific strain and carrier concentration is challenging to realize experimentally. Therefore, further research on the proposed halide perovskite can investigate the combined effects of strain and defects, explore anisotropic strain conditions (e.g., uniaxial or biaxial strain), and consider additional band structure engineering strategies like alloying or doping. We believe that the present study will pave the way for future experimental thermoelectric energy harvesting studies on this material, which will help society to move towards net zero target with better economy.

REFERENCES

- [1] Md. Ferdous Rahman, P. Barman, Md. Azizur Rahman, M. Mushtaq, Md. Rasidul Islam, Md. Atikur Rahman, Md.Z. Sultan, A.R. Chaudhry, A. Irfan, Electronic, optical, thermophysical, and mechanical properties of lead-free Ba₃SbBr₃ perovskite, *Polyhedron* 254 (2024) 116937. <https://doi.org/10.1016/j.poly.2024.116937>.
- [2] T. Mori, S. Priya, Materials for energy harvesting: At the forefront of a new wave, *MRS Bull.* 43 (2018) 176–180. <https://doi.org/10.1557/mrs.2018.32>.
- [3] C. Tong, Emerging Materials for Energy Harvesting, in: *Introduction to Materials for Advanced Energy Systems*, Springer International Publishing, Cham, 2019: pp. 719–817. https://doi.org/10.1007/978-3-319-98002-7_11.
- [4] M. Massetti, F. Jiao, A.J. Ferguson, D. Zhao, K. Wijeratne, A. Würger, J.L. Blackburn, X. Crispin, S. Fabiano, Unconventional Thermoelectric Materials for Energy Harvesting and Sensing Applications, *Chem. Rev.* 121 (2021) 12465–12547. <https://doi.org/10.1021/acs.chemrev.1c00218>.
- [5] X. Zhu, Y. Yu, F. Li, A review on thermoelectric energy harvesting from asphalt pavement: Configuration, performance and future, *Construction and Building Materials* 228 (2019) 116818. <https://doi.org/10.1016/j.conbuildmat.2019.116818>.
- [6] T.M. Tritt, Thermoelectric Phenomena, Materials, and Applications, *Annu. Rev. Mater. Res.* 41 (2011) 433–448. <https://doi.org/10.1146/annurev-matsci-062910-100453>.
- [7] G. Tan, M. Ohta, M.G. Kanatzidis, Thermoelectric power generation: from new materials to devices, *Phil. Trans. R. Soc. A.* 377 (2019) 20180450. <https://doi.org/10.1098/rsta.2018.0450>.
- [8] G.J. Snyder, E.S. Toberer, Complex thermoelectric materials, *Nature Mater* 7 (2008) 105–114. <https://doi.org/10.1038/nmat2090>.
- [9] T. Zhu, Y. Liu, C. Fu, J.P. Heremans, J.G. Snyder, X. Zhao, Compromise and Synergy in High-Efficiency Thermoelectric Materials, *Advanced Materials* 29 (2017) 1605884. <https://doi.org/10.1002/adma.201605884>.
- [10] Sangeeta, M. Singh, Computational study of the thermoelectric properties and lattice dynamics of Li₂MN₂ (M = Zr or Hf), *Materials Research Bulletin* 172 (2024) 112650. <https://doi.org/10.1016/j.materresbull.2023.112650>.
- [11] R. Kumar, R. Kumar, A. Vij, M. Singh, A first-principle study of electronic, thermoelectric, and optical properties of sulfur doped c-HfO₂, *Phys. Scr.* 97 (2022) 075813. <https://doi.org/10.1088/1402-4896/ac7678>.
- [12] Sangeeta, R. Kumar, M. Singh, In-silico realization of YX (X = N, P, As) pnictide monolayers as highly efficient thermoelectric materials, *Surfaces and Interfaces* 55 (2024) 105442. <https://doi.org/10.1016/j.surfin.2024.105442>.

- [13] Md.N. Hasan, H. Wahid, N. Nayan, M.S. Mohamed Ali, Inorganic thermoelectric materials: A review, *Int J Energy Res* 44 (2020) 6170–6222. <https://doi.org/10.1002/er.5313>.
- [14] H. Wang, W. Su, J. Liu, C. Wang, Recent development of n-type perovskite thermoelectrics, *Journal of Materiomics* 2 (2016) 225–236. <https://doi.org/10.1016/j.jmat.2016.06.005>.
- [15] Sangeeta, R. Kumar, M. Singh, Realizing high thermoelectric performance in p-type RbZn₄P₃ Zintl compound: a first-principles investigation, *J Mater Sci* 57 (2022) 10691–10701. <https://doi.org/10.1007/s10853-022-06953-y>.
- [16] Sangeeta, M. Singh, Augmented thermoelectric performance of LiCaX (X = As, Sb) Half Heusler compounds via carrier concentration optimization, *Journal of Physics and Chemistry of Solids* 174 (2023) 111182. <https://doi.org/10.1016/j.jpcs.2022.111182>.
- [17] A. Ghosh, F. Ahmed, Md.J. Ferdous, Mst.M.J. Juhi, M.F.I. Buian, A.A. Miazee, M. Sajid, Md. Maniruzzaman, A.M. Tighezza, M.F. Ahmmed, Md.S. Islam, Strain-induced changes in the electronic, optical and mechanical properties of the inorganic cubic halide perovskite Sr₃PBr₃ with FP-DFT, *Journal of Physics and Chemistry of Solids* 191 (2024) 112053. <https://doi.org/10.1016/j.jpcs.2024.112053>.
- [18] D. Behera, D.R. Lawati, M. Agouri, A. Abbassi, S. Taj, B. Manaut, S.K. Mukherjee, A DFT insight into the physical features of alkaline based perovskite compounds AInBr₃ (A = K, Rb), *Solid State Ionics* 409 (2024) 116513. <https://doi.org/10.1016/j.ssi.2024.116513>.
- [19] B. Akenoun, S. Dahbi, N. Tahiri, O. El Bounagui, H. Ez-Zahraouy, Engineering the optoelectronic and thermoelectric properties of Cs₂BiAgY₆ (Y= Br or Cl) double perovskites through doping with iodine: A DFT study, *Journal of Physics and Chemistry of Solids* 194 (2024) 112229. <https://doi.org/10.1016/j.jpcs.2024.112229>.
- [20] G. Murtaza, I. Ahmad, B. Amin, A. Afaq, M. Maqbool, J. Maqssod, I. Khan, M. Zahid, Investigation of structural and optoelectronic properties of BaThO₃, *Optical Materials* 33 (2011) 553–557. <https://doi.org/10.1016/j.optmat.2010.10.052>.
- [21] M.L. Scullin, C. Yu, M. Huijben, S. Mukerjee, J. Seidel, Q. Zhan, J. Moore, A. Majumdar, R. Ramesh, Anomalously large measured thermoelectric power factor in Sr_{1-x}LaxTiO₃ thin films due to SrTiO₃ substrate reduction, *Appl. Phys. Lett.* 92 (2008) 202113. <https://doi.org/10.1063/1.2916690>.
- [22] J.M.D. Coey, M. Viret, S. Von Molnár, Mixed-valence manganites, *Advances in Physics* 48 (1999) 167–293. <https://doi.org/10.1080/000187399243455>.
- [23] A. Ali, A.U. Rahman, G. Rahman, Thermoelectric properties of KCaF₃, *Physica B: Condensed Matter* 565 (2019) 18–24. <https://doi.org/10.1016/j.physb.2019.04.019>.

- [24] S.M. AL-Shomar, M. Liaqat, I. Anmol, A.M. Quraishi, I. Khan, Amina, K. Arshad, U. Turdialiyev, A. Almahri, V. Tirth, A. Algahtani, A.M. Alsuhaibani, Abdullah, M.S. Refat, A. Zaman, Study of structural, electronic, mechanical, optical and thermoelectric properties of As based halide-perovskites Ba_3AsX_3 ($X = F, Cl$): A first-principles insights, *Journal of Materials Research and Technology* 31 (2024) 2450–2460. <https://doi.org/10.1016/j.jmrt.2024.06.218>.
- [25] Md.F. Rahman, Md.H. Rahman, Md.R. Islam, M.K. Hossain, A. Ghosh, Md.S. Islam, Md.M. Islam, Md. Harun-Or-Rashid, H. Albalawi, Q. Mahmood, The optical and electronic properties of inorganic halide perovskite Sr_3NCl_3 under applied biaxial strain, *J Mater Sci* 58 (2023) 13100–13117. <https://doi.org/10.1007/s10853-023-08825-5>.
- [26] A. Algahtani, Amina, F. Rehman, M. Liaqat, N. Juraev, I. Khan, A.M. Alsuhaibani, Abdullah, V. Tirth, M.S. Refat, A. Zaman, Probing the physical properties of Sr_3AsX_3 ($X = F$ and Br) perovskite compounds for prospective solar cell applications employing the DFT framework, *Inorganic Chemistry Communications* 162 (2024) 112186. <https://doi.org/10.1016/j.inoche.2024.112186>.
- [27] I.K.G.G. Apurba, Md.R. Islam, Md.S. Rahman, Md.F. Rahman, J. Park, Tuning the physical properties of inorganic novel perovskite materials Ca_3PX_3 ($X=I, Br$ and Cl): Density function theory, *Heliyon* 10 (2024) e29144. <https://doi.org/10.1016/j.heliyon.2024.e29144>.
- [28] R. Tranås, O.M. Løvvik, K. Berland, Lattice Thermal Conductivity from First Principles and Active Learning with Gaussian Process Regression, (2023). <https://doi.org/10.48550/ARXIV.2309.06786>.
- [29] C. Hadenfeldt, P. Schulz, Darstellung, Struktur und Temperaturabhängigkeit der Phasenbreite der Phase $Ca_{2-x}As_{1-x}Br_{1+x}$ und thermisches Verhalten der Verbindung Ca_3AsBr_3 , *Zeitschrift Anorg Allge Chemie* 518 (1984) 77–86. <https://doi.org/10.1002/zaac.19845181108>.
- [30] Md.A. Ul Islam, O. Das, D.B. Khadka, Md.R. Islam, Md.F. Rahman, S. Kato, T. Soga, Effect of Low to High Pressure on the Structural, Mechanical, Electrical, and Optical Properties of Inorganic Material Ca_3AsBr_3 : An Ab Initio Investigation, *ACS Omega* (2024) acsomega.3c08131. <https://doi.org/10.1021/acsomega.3c08131>.
- [31] M.F.I. Buian, Most.S. Islam Ria, A. Ghosh, Md.A. Rahman, M.S. Hossain, M.F. Ahmed, A.A. Miazee, M.M.R. Sonic, H.A. Alrafai, A novel investigation into strain-induced changes in the physical properties and solar cell performances of lead-free Ca_3NCl_3 perovskite, *Materials Science in Semiconductor Processing* 180 (2024) 108580. <https://doi.org/10.1016/j.mssp.2024.108580>.
- [32] Md.F. Rahman, Md.A. Rahman, Md.R. Islam, A. Ghosh, Md.A. Bashar Shanto, M. Chowdhury, Md. Al Ijazul Islam, Md.H. Rahman, M.K. Hossain, M.A. Islam, Unraveling the strain-induced and spin–orbit coupling effect of novel inorganic

halide perovskites of Ca₃AsI₃ using DFT, *AIP Advances* 13 (2023) 085329. <https://doi.org/10.1063/5.0156961>.

[33] A. Yadav, S. Kumar, M. Muruganathan, R. Kumar, Thermoelectric properties of half Heusler topological semi-metal LiAuTe, *EPL* 132 (2020) 67003. <https://doi.org/10.1209/0295-5075/132/67003>.

[34] P. Blaha, K. Schwarz, F. Tran, R. Laskowski, G.K.H. Madsen, L.D. Marks, WIEN2k: An APW+lo program for calculating the properties of solids, *The Journal of Chemical Physics* 152 (2020) 074101. <https://doi.org/10.1063/1.5143061>.

[35] K. Schwarz, P. Blaha, G.K.H. Madsen, Electronic structure calculations of solids using the WIEN2k package for material sciences, *Computer Physics Communications* 147 (2002) 71–76. [https://doi.org/10.1016/S0010-4655\(02\)00206-0](https://doi.org/10.1016/S0010-4655(02)00206-0).

[36] J.P. Perdew, K. Burke, M. Ernzerhof, Generalized Gradient Approximation Made Simple, *Phys. Rev. Lett.* 77 (1996) 3865–3868. <https://doi.org/10.1103/PhysRevLett.77.3865>.

[37] F. Tran, P. Blaha, Accurate Band Gaps of Semiconductors and Insulators with a Semilocal Exchange-Correlation Potential, *Phys. Rev. Lett.* 102 (2009) 226401. <https://doi.org/10.1103/PhysRevLett.102.226401>.

[38] G.K.H. Madsen, J. Carrete, M.J. Verstraete, BoltzTraP2, a program for interpolating band structures and calculating semi-classical transport coefficients, *Computer Physics Communications* 231 (2018) 140–145. <https://doi.org/10.1016/j.cpc.2018.05.010>.

[39] G. Kresse, J. Furthmüller, Efficiency of ab-initio total energy calculations for metals and semiconductors using a plane-wave basis set, *Computational Materials Science* 6 (1996) 15–50. [https://doi.org/10.1016/0927-0256\(96\)00008-0](https://doi.org/10.1016/0927-0256(96)00008-0).

[40] A.M. Ganose, J. Park, A. Faghaninia, R. Woods-Robinson, K.A. Persson, A. Jain, Efficient calculation of carrier scattering rates from first principles, *Nat Commun* 12 (2021) 2222. <https://doi.org/10.1038/s41467-021-22440-5>.

[41] S. Ramawat, S. Kukreti, A. Dixit, β - SrZrS₃: A superior intermediate temperature thermoelectric through complex band geometry and ultralow lattice thermal conductivity, *Phys. Rev. Materials* 7 (2023) 085403. <https://doi.org/10.1103/PhysRevMaterials.7.085403>.

[42] A. Togo, First-principles Phonon Calculations with Phonopy and Phono3py, *J. Phys. Soc. Jpn.* 92 (2023) 012001. <https://doi.org/10.7566/JPSJ.92.012001>.

[43] A. Gilani, Nasarullah, S.A. Aldaghfag, M. Yaseen, Magnetic, optical, electronic, structural and thermoelectric features of A₂MgS₄ (A=Sm, Tb): A DFT study, *Journal of Physics and Chemistry of Solids* 175 (2023) 111208. <https://doi.org/10.1016/j.jpcs.2022.111208>.

- [44] T. Katsura, Y. Tange, A Simple Derivation of the Birch–Murnaghan Equations of State (EOSs) and Comparison with EOSs Derived from Other Definitions of Finite Strain, *Minerals* 9 (2019) 745. <https://doi.org/10.3390/min9120745>.
- [45] C. Hadenfeldt, Darstellung und Eigenschaften von Ca_2AsBr , Sr_2AsCl und Ca_3AsBr_3 .: Preparation and Properties of Ca_2AsBr , Sr_2AsCl , and Ca_3AsBr_3 , *Zeitschrift Für Naturforschung B* 31 (1976) 408–410. <https://doi.org/10.1515/znb-1976-0403>.
- [46] M. Mushtaq, M.A. Sattar, S.A. Dar, Phonon phase stability, structural, mechanical, electronic, and thermoelectric properties of two new semiconducting quaternary Heusler alloys CoCuZRZ ($Z = \text{Ge}$ and Sn), *Int J Energy Res* 44 (2020) 5936–5946. <https://doi.org/10.1002/er.5373>.
- [47] I. Waller, *Dynamical Theory of Crystal Lattices* by M. Born and K. Huang, *Acta Cryst* 9 (1956) 837–838. <https://doi.org/10.1107/S0365110X56002370>.
- [48] R. Hill, The Elastic Behaviour of a Crystalline Aggregate, *Proc. Phys. Soc. A* 65 (1952) 349–354. <https://doi.org/10.1088/0370-1298/65/5/307>.
- [49] K.S. Rana, R. Gupta, D. Sarkar, N.K. Singh, S. Acharya, S. Vitta, C. Bera, K. Biswas, A. Soni, Interaction of acoustic and optical phonons in a soft-bonded Cu-Se framework of large unit cell minerals with anionic disorders, *Phys. Rev. B* 108 (2023) 045202. <https://doi.org/10.1103/PhysRevB.108.045202>.
- [50] H.S. Patel, V.A. Dabhi, A.M. Vora, Advancing thermoelectric potential: strontium telluride under compression strain analyzed with HSE hybrid functional and Wannier interpolation, *Sci Rep* 14 (2024) 20700. <https://doi.org/10.1038/s41598-024-55519-2>.
- [51] M. Dutta, T. Ghosh, K. Biswas, Electronic structure modulation strategies in high-performance thermoelectrics, *APL Materials* 8 (2020) 040910. <https://doi.org/10.1063/5.0002129>.
- [52] D. Behera, T.A. Geleta, I. Allaoui, M. Khuli, S.K. Mukherjee, B. Akila, S. Al-Qaisi, First-principle analysis of optical and thermoelectric properties in alkaline-based perovskite compounds AInCl_3 ($A = \text{K}, \text{Rb}$), *Eur. Phys. J. Plus* 139 (2024) 127. <https://doi.org/10.1140/epjp/s13360-024-04921-w>.
- [53] M. Jonson, G.D. Mahan, Mott’s formula for the thermopower and the Wiedemann-Franz law, *Phys. Rev. B* 21 (1980) 4223–4229. <https://doi.org/10.1103/PhysRevB.21.4223>.
- [54] A. Togo, L. Chaput, I. Tanaka, Distributions of phonon lifetimes in Brillouin zones, *Phys. Rev. B* 91 (2015) 094306. <https://doi.org/10.1103/PhysRevB.91.094306>.
- [55] S. Mahmud, M.A. Ali, M.M. Hossain, M.M. Uddin, DFT mediated X_2AuYZ_6 ($X = \text{Cs}, \text{Rb}$; $Z = \text{Cl}, \text{Br}, \text{I}$) double Perovskites for photovoltaic and wasted heat management device applications, (2024). <https://doi.org/10.48550/ARXIV.2404.15693>.

[56] ‘Density functional theory’, Wikipedia

[57] <https://www.cambridge.org/core/books/electronicstructure/DDFE838DED61D7A402FDF20D735BC63A>

[58] https://www.vasp.at/wiki/index.php/Category:Exchange-correlation_functionals

[59] Harald Ibach, Hans Lüth, ‘Solid-State Physics’, Springer

[60] <https://www.vasp.at/info/about/>

[61] Georg K.H. Madsen, Jesús Carrete, Matthieu J. Verstraete, ‘BoltZTraP2, a program for interpolating band structures and calculating semi-classical transport coefficients’, 2018, Elsevier, Computer Physics Communications.

[62] <https://hackingmaterials.lbl.gov/amset/>

PROOF AND SCOPUS INDEXING

Physics letters A Sort By: Relevancy

Active Filters 1

SCIENCE CITATION INDEX EXPANDED (SCIE) ×

Search Results

Found 930 results (Page 1) [Share These Results](#)

Exact Match Found

PHYSICS LETTERS A

Publisher: ELSEVIER, RADARWEG 29, AMSTERDAM, Netherlands, 1043 NX
ISSN / eISSN: 0375-9601 / 1873-2429
Web of Science Core Collection: Science Citation Index Expanded
Additional Web of Science Indexes: Current Contents Physical, Chemical & Earth Sciences | Essential Science Indicators

[Share This Journal](#) [View profile page](#)

* Requires free login.



ELSEVIER City of Geology University of London, London, United Kingdom

Journals & Books [Help](#) [Search](#) [My account](#) [Sign in](#)



Physics Letters A

Supports open access

4.5

CiteScore

2.3

Impact Factor

[Articles & Issues](#) [About](#) [Publish](#) [Order journal](#) [Search in this journal](#) [Submit your article](#) [Guide for authors](#)

About the journal



Letter

Optimizing thermoelectric performance of halide perovskite Ca_3AsBr_3 through strain engineering

Sumedha Yadav, Sangeeta, Kulwinder Kumar, Mukhtiyar Singh ^{*}

Computational Quantum Materials Design (CQMD) Laboratory, Department of Applied Physics, Delhi Technological University, Delhi 110042, India

ARTICLE INFO

Communicated By: Lilia Woods

Keywords:
DFT
Halide perovskites
Thermoelectric properties
Lattice thermal conductivity
Figure of merit

ABSTRACT

We investigate structural, dynamical, elastic, electronic, and thermoelectric properties of cubic perovskite halide Ca_3AsBr_3 under the effect of strain using first-principles calculations. It is found to have a direct bandgap of 2.425 eV that further reduces under compressive strain making it an ideal candidate for thermoelectric application. The material satisfies various stability criteria, e.g., dynamical, thermodynamical, and mechanical. The transport calculations show the highest Seebeck coefficient of value $-158.227 \mu\text{VK}^{-1}$ at 700 K for *n*-type Ca_3AsBr_3 unstrained structure at carrier concentration $1 \times 10^{21} \text{cm}^{-3}$, which is further enhanced to $-482.366 \mu\text{VK}^{-1}$ for -2 % strain. The lattice thermal conductivity of the material is reduced from $1.243 \text{Wm}^{-1}\text{K}^{-1}$ to $0.627 \text{Wm}^{-1}\text{K}^{-1}$ at 700 K under 3 % strain. This low thermal conductivity, coupled with positive power factor values, results in increased peak thermoelectric figure of merit from 0.36 (unstrained) to 0.56 (+3 % strain) at 700 K for an *n*-type doping concentration of $1 \times 10^{20} \text{cm}^{-3}$.

1. Introduction

As global energy consumption continues to rise, the conventional energy sources becoming unprecedently more pressing. Moreover, the depletion of conventional fossil fuels and their environmental impact raises serious concerns about long-term sustainability. This challenge makes it essential to explore alternative, renewable energy solutions that can support future energy needs while minimizing ecological harm [1–5]. Thermoelectric (TE) materials represent one of the most promising avenues for sustainable energy conversion. These materials can harness useful electricity from waste heat and thus have been a research focus in recent years [6]. The efficiency of a TE material is given by a dimensionless quantity known as the Figure of Merit (FOM), which is defined by $ZT = \frac{S^2\sigma}{\kappa_e + \kappa_l}$ where S represents the Seebeck coefficient, σ is the electrical conductivity, κ_e is the electronic thermal conductivity, and κ_l is the lattice thermal conductivity. In order to obtain a high ZT , high S , high σ , and a low thermal conductivity (κ) are required [7,8]. However, these parameters have very strong intercoupling, and it is very challenging to increase the ZT of conventional TE materials [9]. To decouple these coefficients, researchers have opted for many strategies [8,10–12]. The inorganic materials like Bi_2Te_3 (effective at room temperature), chalcogenides and half Heusler compounds (suited for mid-to-high temperatures like 400–800 K), skutterudites and clathrates (500–900

K), Zintl phases (covering various temperature ranges for different compositions ~300–900 K), and oxide perovskites (best for high temperatures ~700–1200 K) are widely used as efficient TE materials across different temperature regimes [13–16]. However, the scarcity of raw materials such as tellurium and lead, along with the complex and costly fabrication processes, significantly hinder the commercialization of such inorganic TE materials.

Inorganic perovskites are low-cost efficient materials emerging as promising materials in science and technology development [17]. Owing to their unique crystal structure ABX_3 (with A, and B as cations of different sizes and X as an anion that bonds with both cations) perovskite materials are widely used in chemistry, physics, and other fields with successful synthesis of hundreds of distinct materials that make up the large perovskite family including conductors, semiconductors, and insulators [18]. These perovskites reveal many intriguing properties such as high TE power, ferroelectricity, superconductivity, spin-dependent transport, etc. [19–23]. Further, exploring alternative perovskite frameworks A_3BX_3 such as Sr_3NCl_3 , Ca_3PX_3 , and Sr_3PBr_3 , which naturally exhibit cubic symmetry like traditional ABX_3 perovskites, offers several advantages, including greater structural stability, improved tunability of electronic, and optical properties and can show great promise for TE applications [24–27]. For instance, BaAsX_3 ($X = \text{F}, \text{Cl}$) has demonstrated ZT values of 0.92 and 0.82, respectively, which

* Corresponding author.

E-mail address: mukhtiyarsingh@dtu.ac.in (M. Singh).<https://doi.org/10.1016/j.physleta.2025.130625>

Received 18 March 2025; Received in revised form 1 May 2025; Accepted 4 May 2025

Available online 5 May 2025

0375-9601/© 2025 Elsevier B.V. All rights are reserved, including those for text and data mining, AI training, and similar technologies.

PLAGIARISM



Page 1 of 69 - Cover Page

Submission ID trn:oid::27535:99842489

Sumedha Thesis.docx

 Delhi Technological University

Document Details

Submission ID
trn:oid::27535:99842489

Submission Date
Jun 8, 2025, 2:21 PM GMT+5:30

Download Date
Jun 8, 2025, 2:54 PM GMT+5:30

File Name
Sumedha Thesis.docx

File Size
12.1 MB

65 Pages
12,267 Words
70,960 Characters



Page 1 of 69 - Cover Page

Submission ID trn:oid::27535:99842489

7% Overall Similarity

The combined total of all matches, including overlapping sources, for each database.

Filtered from the Report

- Bibliography
- Small Matches (less than 14 words)

Exclusions

- 81 Excluded Matches

Match Groups

- 20 Not Cited or Quoted 6%**
Matches with neither in-text citation nor quotation marks
- 2 Missing Quotations 1%**
Matches that are still very similar to source material
- 0 Missing Citation 0%**
Matches that have quotation marks, but no in-text citation
- 0 Cited and Quoted 0%**
Matches with in-text citation present, but no quotation marks

Top Sources

- 5% Internet sources
- 6% Publications
- 1% Submitted works (Student Papers)

Integrity Flags

1 Integrity Flag for Review

- Replaced Characters**
47 suspect characters on 15 pages
Letters are swapped with similar characters from another alphabet.

Our system's algorithms look deeply at a document for any inconsistencies that would set it apart from a normal submission. If we notice something strange, we flag it for you to review.

A Flag is not necessarily an indicator of a problem. However, we'd recommend you focus your attention there for further review.